

Spontaneous symmetry breakings in graphene subjected to in-plane magnetic field

I.L. Aleiner,¹ D. E. Kharzeev,² and A. M. Tsvelik^{3,4}

¹ *Physics Department, Columbia University, New York, NY 10027, USA*

² *Department of Physics, Brookhaven National Laboratory, Upton, NY 11973-5000, USA*

³ *Department of Condensed Matter Physics and Materials Science,
Brookhaven National Laboratory, Upton, NY 11973-5000, USA*

⁴ *Department of Physics and Astronomy, SUNY at Stony Brook, Stony Brook, NY 11794-3800, USA*

(Dated: November 7, 2018)

Application of the magnetic field parallel to the plane of the graphene sheet leads to the formation of electron- and hole-like Fermi surfaces. Such situation is shown to be unstable with respect to the formation of an excitonic condensate even for an arbitrary weak magnetic field and interaction strength. At temperatures lower than the mean-field temperature the order parameter amplitude is formed. The order parameter itself is a $U(2)$ matrix allowing for the combined rotations in the spin and valley spaces. These rotations smoothly interpolate between site and bond centered spin density waves and spin flux states. The trigonal warping, short range interactions, and the three particle Umklapp processes freeze some degrees of freedom at temperatures much smaller than the mean-field transition temperature and make either Berezinskii-Kosterlitz-Thouless (driven either by vortices or half-vortices) or Ising type transitions possible. Strong logarithmic renormalization for the coupling constants of these terms by the Coulomb interaction are calculated within one-loop renormalization group. It is found that in the presence of the Coulomb interaction some short range interaction terms become much greater than one might expect from the naive dimensionality counting.

PACS numbers: 73.63.-b, 81.05.Uw, 72.15.Rn

I. INTRODUCTION

The fabrication of the graphene (graphite monolayers)^{1,2} and subsequent observation of the Integer Quantum Hall^{3,4} in this layer produced a splash of theoretical and experimental activity.

Though the transport properties of graphene are controlled by the impurities, it is still worthwhile to understand the phase diagram of the completely clean graphene.

The main purpose of this paper is to point out that an application of magnetic field in graphene plane facilitates a spontaneous symmetry breaking. Though the dimensionless Coulomb coupling e^2/hv in graphene is large at large energies, it undergoes strong downward renormalization at small energies so that the analysis for weak magnetic fields can be safely carried out without resorting to any uncontrollable approximations⁵.

To achieve this goal and understand the effects of the naively dimensionally irrelevant terms (such as trigonal warping, short range part of the interaction, Umklapp terms) we considered their logarithmic renormalization by the long-range Coulomb interaction and found some un-expected results. Earlier the effect of the Coulomb interaction was considered for the isotropic terms only⁶⁻⁸.

The remainder of the paper is organized as follows. In Section II we discuss symmetries of a two-dimensional graphene sheet and write down its low energy Hamiltonian. In Section III we describe physical reasons for the instability and suggest the order parameter. In Section IV we write down the Landau-Ginzburg free energy functional, discuss thermal fluctuations and describe the

phase diagram. Section V is devoted to the analysis of the microscopics: we study the energy dependence of the effective coupling and renormalization of the leading anisotropies in graphene. Section VI contains the summary and conclusions. Some auxiliary material is relegated into two Appendices.

II. SYMMETRIES OF THE SYSTEM AND THE MODEL LOW ENERGY HAMILTONIAN.

The purpose of this section is to write down the low energy energy field theory to describe the electron-electron interaction in graphene. Our consideration will be based on the discrete symmetries of the lattice only and we will not appeal to any microscopic model⁹.

The effective low energy field theory of graphene is constructed by the factorization of the original fermionic fields $\Psi_\sigma(\mathbf{r}; \tau)$, $\sigma = \uparrow, \downarrow$ in terms of the oscillatory Bloch functions corresponding to the K, K' points of the Brillouin zone, see Fig. 1,

$$\Psi_\sigma(\mathbf{r}; \tau) = \vec{\psi}_\sigma(\mathbf{r}, \tau) * \vec{u}(\mathbf{r}). \quad (2.1)$$

where $\psi_\sigma(\mathbf{r}, \tau)$ is the four component fermionic field which can vary only over distances much larger than the lattice constant, and $\vec{u}(\mathbf{r})$ is the four-dimensional vector of the Bloch functions whose structure is described below.

Consider the Bloch functions $(u^A(\mathbf{r})_K, u^B(\mathbf{r})_K)$ forming a basis for two-dimensional irreducible representation of the wave-vector symmetry group C_{3v} . (In the

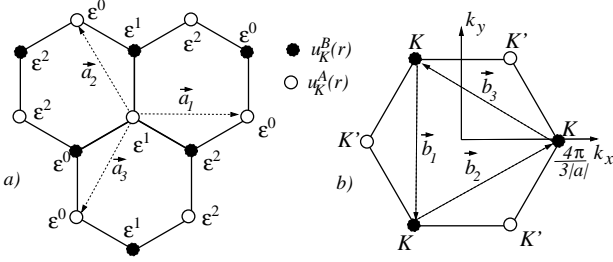


FIG. 1: a) The hexagonal lattice of graphene with the shortest translation vectors $\vec{a}_{1,2,3}$. Circles shows the positions of the maxima of the absolute values of Bloch functions $u_{K}^{A,B}(\mathbf{r})$. Their relative phases are shown, $\epsilon = \exp(i2\pi/3)$. b) The first Brillouin zone and the shortest translation vectors of the reciprocal lattice $\vec{b}_{1,2,3}$. Two non-equivalent Dirac cones are formed in the vicinity of points K and K' .

tight-binding picture those Bloch functions are peaked on the corresponding sub-lattices, see Fig. 1). The overall point symmetry group is C_{6v} and thus the wave-functions $u_{K'}^A = [u_K^A]^*$, $u_{K'}^B = [u_K^B]^*$ also have to be included as points K', K are connected to each other by C_2 rotation and by time reversal symmetry.

They are conveniently joined in a vector¹⁰

$$\vec{u}^T = ((u_K^A; u_K^B)_{AB} (u_{K'}^B; -u_{K'}^A)_{AB})_{KK'} \quad (2.2)$$

forming the basis of the four-dimensional irreducible representation of the planar symmetry group of graphene $\sum_{j_1, j_2} C_6^{v j_1} \vec{a}_1 + j_2 \vec{a}_2$, with the normalization condition

$$\int_{uc} d\mathbf{r} \vec{u}(\mathbf{r}) \cdot \vec{u}^*(\mathbf{r}) = 4|\vec{a}_1 \times \vec{a}_2|. \quad (2.3)$$

Hereinafter, \int_{uc} denotes integration within the unit cell.

Thus, the fermionic field describing all relevant degrees of freedom, $\psi^T = (\psi_\uparrow, \psi_\downarrow)$, has eight components. This eight-dimensional space is represented, see Eq. (2.2), as a direct product of the valley, (KK') , the sub-lattice, (AB) , and the spin, (s) , two-dimensional spaces. We will use standard 2×2 Pauli matrices $\hat{\tau}_{x,y,z}$, with the corresponding subscripts to parametrize all 8×8 matrices describing the Hamiltonian and the symmetry properties

The partition function describing the low energy properties of the interacting electrons in a clean graphene is given by ($\hbar = 1$)

$$\mathcal{Z} = \int \mathcal{D}\psi^\dagger \mathcal{D}\psi \exp \left[- \int_0^{1/T} d\tau \int d\mathbf{x} \left[\psi^\dagger \frac{\partial \psi}{\partial \tau} + H(\psi^\dagger, \psi) \right] \right], \quad (2.4)$$

The Hamiltonian of the system has to satisfy all the discrete symmetries of the clean graphene, and to remain invariant with respect to transformations of the fields generated by the rotation C_3 , two reflections $\sigma_v^{x,y}$, and

translations (t) ;

$$C_3 : \psi(\mathbf{r}) \rightarrow -\exp \left[\theta^C \left(\mathbf{r} \times \nabla + \frac{i}{2} \hat{\Sigma}_z \right) \right] \psi(\mathbf{r}) \quad (2.5a)$$

$$\sigma_v^x : \psi(x, y) \rightarrow \hat{\Sigma}_x \hat{\Lambda}_z \psi(x, -y) \quad (2.5b)$$

$$\sigma_v^y : \psi(x, y) \rightarrow \hat{\Sigma}_z \hat{\Lambda}_x \psi(-x, y) \quad (2.5c)$$

$$t : \psi(\mathbf{r}) \rightarrow \exp \left[i\theta^t \hat{\Lambda}_z \right] \psi(\mathbf{r}). \quad (2.5d)$$

where $\theta^{C,t} = \pm 2\pi/3$. and we introduced the matrices

$$\begin{aligned} \hat{\Sigma}_\alpha &= \hat{\tau}_\alpha^{AB} \otimes \mathbb{1}^{KK'} \otimes \mathbb{1}^s; \quad \hat{\Lambda}_\alpha = \mathbb{1}^{AB} \otimes \hat{\tau}_\alpha^{KK'} \otimes \mathbb{1}^s \\ \hat{S}_\alpha &= \mathbb{1}^{AB} \otimes \mathbb{1}^{KK'} \otimes \hat{\tau}_\alpha^s \end{aligned} \quad (2.6)$$

$\alpha = x, y, z$.

Continuous $U(1)$ rotations in the spin space are given by

$$U(1) : \psi \rightarrow \exp \left(i\theta_s \hat{S}_z / 2 \right) \psi \quad (2.7)$$

where we choose z -direction of the spin to be along the magnetic field.

Time reversal symmetry for the parametrization (2.2) acquires a natural form

$$\mathcal{T} : \psi(\tau) \rightarrow \hat{\tau}_y^{AB} \otimes \hat{\tau}_y^{KK'} \otimes \hat{\tau}_y^s \psi^*(-\tau), \quad \mathcal{B} \rightarrow -\mathcal{B} \quad (2.8)$$

where \mathcal{B} is the magnetic field acting in our case only on electron spin.

Having listed the important symmetries of the problem, we present the Hamiltonian in the form

$$H = H_D + H_C + H_w + H_{sr} + H_u. \quad (2.9)$$

The first term describes the Dirac-type kinetic energy and the Zeeman energy

$$H_D = -iv(r_c) \psi^\dagger \nabla \cdot \hat{\Sigma} \psi + \mathcal{B} \psi^\dagger \hat{S}_z \psi. \quad (2.10)$$

where $\nabla = (\partial_x, \partial_y)$, $\hat{\Sigma}$ is defined in Eq. (2.6), the Bohr magneton and the g -factor are included into the definition of \mathcal{B} , and r_c is the minimal linear scale present in the problem. As it was pointed out in Ref. 6 (see also Refs. 7,8), the velocity $v(r_c)$ becomes scale dependent due to the Coulomb interaction

$$H_C = \frac{e^2}{2} \int d\mathbf{r}_1 \frac{(\psi^\dagger(\mathbf{r})\psi(\mathbf{r})) (\psi^\dagger(\mathbf{r}_1)\psi(\mathbf{r}_1))}{|\mathbf{r} - \mathbf{r}_1|}, \quad (2.11)$$

whose strength e^2 cannot be renormalized as it is the only nonlocal term in the system.

Though the terms described by Eqs. (2.10) and (2.11) are the most important ones on the dimensional grounds, they are not sufficient to define the problem completely

since their symmetries are much higher than of (2.5):

$$C_\infty : \psi(\mathbf{r}) \rightarrow \exp \left[\theta^C \left(\mathbf{r} \times \nabla + \frac{i}{2} \hat{\Sigma}_z \right) \right] \psi(\mathbf{r}) \quad (2.12a)$$

$$\sigma_v : \psi(x, y) \rightarrow \hat{\Sigma}_x \psi(x, -y) \quad (2.12b)$$

$$U(1) \otimes SU(2) \otimes SU(2) : \psi(\mathbf{r}) \rightarrow \hat{U}(\alpha^\pm, \theta^s; \mathbf{n}_{1,2}) \psi(\mathbf{r}),$$

$$\hat{U} = \exp \left[\frac{i\alpha^- \mathbf{n}_2 \cdot \vec{\Lambda} \hat{S}_z}{2} \right] \exp \left[\frac{i\theta^s \hat{S}_z}{2} \right] \exp \left[\frac{i\alpha^+ \mathbf{n}_1 \cdot \vec{\Lambda}}{2} \right] \quad (2.12c)$$

than it is allowed by Eqs. (2.5)–(2.8). Here θ^i are the continuous real variables and $\mathbf{n}_{1,2}$ are three-dimensional unit vectors.

The terms lowering the symmetry of the Hamiltonian can appear both in the kinetic energy and in the interaction Hamiltonian. For instance, the trigonal warping of the one-electron spectrum is given by

$$H_w = \lambda_w(r_c) r_c v(r_c) \psi^\dagger \left[\partial_+^2 \hat{\Sigma}_+ \hat{\Lambda}_z + h.c. \right] \psi \quad (2.13)$$

where $\partial_+ \equiv \partial_x + i\partial_y$, $\hat{\Sigma}_+ \equiv (\hat{\Sigma}_x + i\hat{\Sigma}_y)/2$. Dimensionless coupling $\lambda_w(r_c)$ is of the order of unity at r_c of the order of the lattice constant and scales down at larger distances.

In writing down the short-range interaction, one can neglect the effect of the Zeeman term on the scale of the order of the lattice constant. Thus the $SU(2)$ invariance in the spin space must be preserved and ¹

$$\begin{aligned} \frac{2}{r_c v(r_c)} H_{sr} &= \sum_{\alpha, \beta = x, y, z} F_{\alpha\beta}(r_c) (\psi^\dagger \Sigma_\alpha \Lambda_\beta \psi)^2 \quad (2.14a) \\ &+ \sum_{\alpha = x, y, x} \left[J_\alpha^\Sigma(r_c) (\psi^\dagger \Sigma_\alpha \psi)^2 + J_\alpha^\Lambda(r_c) (\psi^\dagger \Lambda_\alpha \psi)^2 \right]. \end{aligned}$$

The symmetries (2.5) immediately yield the relation

$$\begin{aligned} F_{zz} &= 2F_-^z + F_+^z; \quad F_{xz} = F_{yz} = -F_-^z + F_+^z; \\ F_{zx} &= F_{zy} = 2F_-^\perp + F_+^\perp; \quad (2.14b) \\ F_{xx} &= F_{yy} = F_{xy} = F_{yx} = -F_-^\perp + F_+^\perp; \\ J_z^{\Sigma, \Lambda} &= 2J_-^{\Sigma, \Lambda} + J_+^{\Sigma, \Lambda}; \quad J_x^{\Sigma, \Lambda} = J_y^{\Sigma, \Lambda} = -J_-^{\Sigma, \Lambda} + J_+^{\Sigma, \Lambda}. \end{aligned}$$

A reason for introducing F_\pm, J_\pm couplings will become clear later in Sec. V. As for the numerical values of the couplings, a very crude estimate at the scale r_c of the order of the lattice constants can be obtained by calculating the matrix elements of the bare interaction potential:

$$\begin{aligned} F_{\alpha\beta} &= \left(\frac{e^2}{4v(r_c)} \right) \int dr_1 \int_{uc} \frac{dr_2 \rho_{\alpha\beta}(\mathbf{r}_1) \rho_{\alpha\beta}(\mathbf{r}_2)}{r_c |\vec{a}_1 \times \vec{a}_2| |r_1 - r_2|} \quad (2.15) \\ \rho_{\alpha\beta}(\mathbf{r}) &\equiv (\vec{u}(\mathbf{r})^\dagger \Sigma_\alpha \Lambda_\beta \vec{u}(\mathbf{r})), \end{aligned}$$

and $J^{\Sigma, \Lambda} = 0$. (Obtaining finite values of $J^{\Sigma, \Lambda}$ requires the virtual processes at least of the second order.) As $\rho_{\alpha\beta}(\mathbf{r})$ contains only oscillatory components, see Eqs. (2.2) and (2.6), the integral in Eq. (2.15) is determined only by the distances of the order of the lattice constant. Thus, the parameters are extremely sensitive to the details at short distances and should be treated as entries for the low-energy theory.

Though the warping and the short range interaction (2.13)–(2.14) lift most of the spurious symmetries (2.12), the extra continuous $U(1)$ symmetry is still present corresponding to Eq. (2.5d) with continuous θ^t . It is related to conservation of quasimomentum which is violated only by the Umklapp processes. The lowest order term satisfying the symmetries (2.5) has the form

$$\begin{aligned} H_u &= \frac{r_c^3 v(r_c)}{6} \sum_{\alpha\beta\gamma} \mathcal{F}_{\alpha\beta\gamma}(r_c) \quad (2.16) \\ &\times \left[(\psi^\dagger \Sigma_\alpha \hat{\Lambda}_+ \psi) (\psi^\dagger \Sigma_\beta \hat{\Lambda}_+ \psi) (\psi^\dagger \Sigma_\gamma \hat{\Lambda}_+ \psi) + h.c. \right] \end{aligned}$$

where $\hat{\Lambda}_+ \equiv (\hat{\Lambda}_x + i\hat{\Lambda}_y)/2$, $\mathcal{F}_{\alpha\beta\gamma}$ is symmetric with respect to permutations of the indices and

$$\begin{aligned} \mathcal{F}_{xyz} &= 0; \quad \mathcal{F}_{zzz} = 2\mathcal{F}_- + \mathcal{F}_+; \\ \mathcal{F}_{zxx} &= \mathcal{F}_{zyy} = -\mathcal{F}_- + \mathcal{F}_+. \quad (2.17) \end{aligned}$$

Finally, we notice that all the listed terms (2.10)–(2.16) remain invariant under the electron-hole transformation

$$e - h : \quad \psi \rightarrow \hat{\Sigma}_z \hat{S}_x \psi^*. \quad (2.18)$$

This electron-hole correspondence will be important for the discussion of the instability arising in the in-plane magnetic field which we will discuss now².

III. PHYSICAL REASONS FOR THE INSTABILITY AND THE ORDER PARAMETER

Having established the form of the Hamiltonian consistent with the symmetries of the lattice, we turn to the qualitative discussion of the instability and determine the target space of the order parameter. The symmetry arguments will allow us to do this without any actual calculation,

Assume that no symmetries are broken at $\mathcal{B} = 0$. Then, the low lying excitations are fermionic electron- and hole- like excitations with spin 1/2 and the dispersion $\epsilon(k) = v(|k|)|k|$ as shown in Fig. 2 (a). The magnetic field parallel to the plane acts only on the spin and hence shifts the spectrum of the excitations making the creation of the Fermi seas for the electrons and holes energetically

¹ All the other short range spin rotational invariant interaction terms can be reduced to those of Eqs. (2.14) by using the identity $2\delta_{\sigma_1\sigma_2}\delta_{\sigma_3\sigma_4} = \delta_{\sigma_1\sigma_4}\delta_{\sigma_2\sigma_3} + \hat{\tau}_{\sigma_1\sigma_4}\hat{\tau}_{\sigma_2\sigma_3}$.

² The leading irrelevant term lifting the e-h symmetry $\propto \nabla \psi^\dagger \nabla \psi$ does not break any other interesting symmetries and will not be important for our purposes.

favorable, Fig. 2 b). As the electrons and holes have the opposite charge, the Coulomb interaction makes them to attract each other. On the other hand, existence of the finite Fermi-surface leads to the Cooper-like instability first discovered in Ref. 11. This instability occurs even for an arbitrary weak interaction potential.

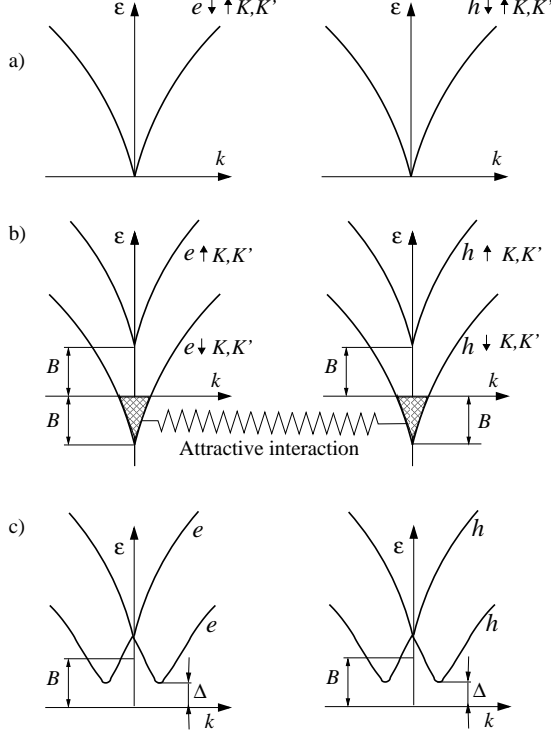


FIG. 2: The mechanism of instability in parallel magnetic field, \mathcal{B} . a) The spectra of the one-particle excitation at $\mathcal{B} = 0$; b) The shift of the spectra by finite \mathcal{B} and the formation of the electron and hole Fermi seas; c) The attractive Coulomb interaction between electrons and holes leads to the instability towards a formation of the excitonic condensate¹¹ creating a gap in the one particle spectrum.

As the result, gap $\Delta_0(T)$ is formed in the one-particle spectrum, Fig. 2 c). The resulting state is incompressible excitonic insulator with gapped charge excitations. The neutral excitations, however, are still quite interesting.

As the electrons and holes can be paired with different phases and different valley indices can be involved, the resulting order parameter has a non-trivial matrix structure which will be discussed now. As the exciton condensate is created by pairing of an electron and a hole with opposite momenta, the order parameter Δ has to be of the form $\langle \psi_e \psi_h \rangle$. On the other hand the electron-hole transformation is defined in Eq. (2.18). Thus, we obtain

$$\hat{\Delta} = \langle \psi \otimes \psi^\dagger \rangle = \Delta_0(T) \hat{\Sigma}_z \hat{S}_x \quad (3.1)$$

Here Δ is 8×8 matrix acting in the space discussed after Eq. (2.3) and the $\hat{\Sigma}_z, \hat{S}_x$ are defined in Eq. (2.6).

If only symmetric terms (2.10) and (2.11) were present, the energy of the system would be invariant with respect

to the replacement $\Delta \rightarrow \hat{U} \Delta \hat{U}^\dagger$. where \hat{U} is given by Eq. (2.12c). Using Eqs. (3.1) and (2.12c), we obtain the most general form of the matrix order parameter

$$\hat{\Delta} = \Delta_0(T) \hat{\tau}_z^{AB} \otimes \hat{Q}, \quad (3.2a)$$

where \hat{Q} is the 4×4 Hermitian matrix acting in spin and valley spaces subjected to the following constraints

$$\begin{aligned} \hat{Q} &= \hat{Q}^\dagger; \quad \hat{Q}^2 = \mathbb{1}^{KK'} \otimes \mathbb{1}^{AB}; \\ \left(\mathbb{1}^{KK'} \otimes \hat{\tau}_z^s \right) \hat{Q} \left(\mathbb{1}^{KK'} \otimes \hat{\tau}_z^s \right) &= -\hat{Q}. \end{aligned} \quad (3.2b)$$

The corresponding mean field single particle spectrum consists of four branches (see Fig. 2c):

$$E_\pm^2 = [\epsilon(k) \pm \mathcal{B}]^2 + |\Delta|^2 \quad (3.2c)$$

In terms of the angles in Eqs. (2.12c), the Q -matrix can be re-written as $(\alpha_-, \mathbf{n}_2 \rightarrow \alpha, \mathbf{n})$

$$\hat{Q} = \mathbb{1}^{KK'} \otimes \left(\mathbf{e}_1 \vec{\tau}^s \right) \cos \alpha + \left(\mathbf{n} \vec{\tau}^{KK'} \right) \otimes \left(\mathbf{e}_2 \vec{\tau}^s \right) \sin \alpha \quad (3.2d)$$

where $\mathbf{e}_{1,2}$ are two mutually orthogonal unit vectors in the plane perpendicular to the spin quantization axis $\mathbf{e}_1 = (\cos \theta_s, \sin \theta_s, 0)$, $\mathbf{e}_2 = (-\sin \theta_s, \cos \theta_s, 0)$.

Another way to parametrize Q from Eq. (3.2b) is to write

$$\hat{Q} = \begin{pmatrix} 0 & \hat{V} \\ \hat{V}^\dagger & 0 \end{pmatrix}_s, \quad \hat{V}^\dagger \hat{V} = \mathbb{1}^{KK'}, \quad (3.2e)$$

where \hat{V} is a unitary 2×2 matrix in the valley space. Therefore, the order parameter is described by $U(2) = SO(3) \times U(1)$ matrices.

Before writing down the effective action or the free energy functional, it is better to explain the physical meaning of different angles in Eq. (3.2d). To do so we will introduce the spin density and the ‘‘spin flux’’, which in terms of the original (not smooth) fermionic fields have the form

$$\vec{s}(\mathbf{r}) = \frac{1}{2} \langle \Psi_\sigma^\dagger(\mathbf{r}) \vec{\tau}_{\sigma\sigma'}^s \Psi_{\sigma'}(\mathbf{r}) \rangle \quad (3.3)$$

$$\vec{\Phi}(\mathbf{r}) = \frac{i}{9} \sum_{j_1, j_2=1}^3 \sin \frac{2\pi j_{12}}{3} \langle \Psi_\sigma^\dagger(\mathbf{r} + \vec{a}_{j_2}) \vec{\tau}_{\sigma\sigma'}^s \Psi_{\sigma'}(\mathbf{r} + \vec{a}_{j_1}) \rangle,$$

where the translation vectors $\vec{a}_{1,2,3}$ are shown on Fig. 1, and $j_{12} = j_1 - j_2$.

Using Eqs. (2.1), (3.1), and (3.2), we find

$$\begin{aligned} \vec{s}(\mathbf{r}) &\propto \mathbf{e}_2 \sin \alpha \left[n_z (|u_A(\mathbf{r})|^2 - |u_B(\mathbf{r})|^2) \right. \\ &\quad \left. + 2n_x \text{Re} u_A(\mathbf{r}) u_B(\mathbf{r}) + 2n_y \text{Im} u_A(\mathbf{r}) u_B(\mathbf{r}) \right]. \end{aligned} \quad (3.4a)$$

The corresponding spin density configurations consistent with the phase factors of the Bloch function of Fig. 1 are shown on Fig. 3 a)-c). Configuration of $\alpha = \pi/2, n_z = 1$

corresponds to the site centered spin density wave. It does not change the periodicity of the original lattice, so the Bragg peaks in the neutron scattering will remain at the same positions $\vec{q} = j_1 \vec{b}_1 + j_2 \vec{b}_2$, and the ordering will affect only their internal structure. On the other hand, $\alpha = \pi/2, n_z = 0$, see Fig. 3 b,c), corresponds to the link centered density waves. It is easy to see that in that case the unit cell is tripled so that additional Bragg peaks at the positions $\vec{q} = \pm K + j_1 \vec{b}_1 + j_2 \vec{b}_2$ will emerge. Rotation in n_x - n_y plane corresponds to a smooth transition between Fig. 3 b,c) configurations. Such smooth rotation can be also understood as a continuous sliding of the superimposed spin-density wave with respect to the crystal lattice.

The spin flux, Fig. 3 d) is maximal at $\alpha = 0, \pi$

$$\vec{\Phi}(\mathbf{r}) \propto \mathbf{e}_1 \cos \alpha (|u_A(\mathbf{r})|^2 - |u_B(\mathbf{r})|^2). \quad (3.4b)$$

Unfortunately, it is not coupled to any obvious physical field which makes its direct experimental observation unlikely.

IV. FREE ENERGY, THERMAL FLUCTUATIONS, AND PHASE DIAGRAM

Order parameter (3.2) allows for smooth rotations between all the states of Fig.3, and thus is subjected to strong thermal fluctuations. Such fluctuations are governed by the Landau free energy functional which we are about to describe.

First we introduce a new definition of Λ, S -matrices Eq. (2.6), as

$$\hat{\Lambda}_\alpha = \hat{\tau}_\alpha^{KK'} \otimes \mathbb{1}^s, \quad \hat{S}_\alpha = \mathbb{1}^{KK'} \otimes \hat{\tau}_\alpha^s, \quad (4.1)$$

where $\alpha = x, y, z$, and $\hat{\Lambda}_\pm \equiv (\hat{\Lambda}_x \pm i \hat{\Lambda}_y)/2$. This modification is convenient because there are no gapless rotations possible in the sub-lattice space after the value of the mean-field order parameter is established.

The only possible form for the free energy compatible with the symmetries of the system (2.5) is given by

$$\mathcal{Z} \propto \sum_v \dots \mu^{N_v} \int \mathcal{D}\hat{Q} \exp \left[-\frac{1}{T} \int d^2\mathbf{r} \mathbb{F} \{ \hat{Q} \} \right]; \quad (4.2)$$

$$\mathbb{F} = \mathbb{F}_\circ + \mathbb{F}_\perp + \mathbb{F}_\triangleright,$$

where symbol $\sum_v \dots \mu^{N_v}$ stands for a summation over the topological defects, see subsection IV A, and μ denotes a fugacity of such defects. A description of the thermodynamics in terms of matrix Q subject to hard constraints (3.2b) is valid only at the distances larger than the spatial scale

$$\xi_{MF} \simeq \frac{v(R_B)}{\Delta_0(T)}, \quad (4.3)$$

where the scale dependence of the velocity and the length R_B is defined in microscopic theory section, see Sec. V.

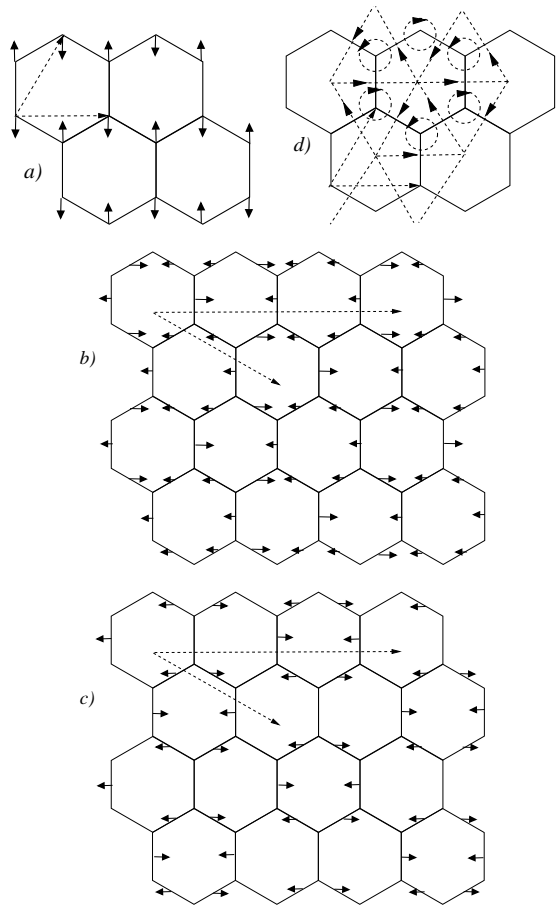


FIG. 3: a)-c) Sketches of the spin density from Eq. (3.4a), for $\alpha = \pi/2$, and a) $n_z = 1$ [$N_4 = 1$ in notation of Eq. (4.5)], b) $n_x = 1$ ($N_2 = 1$) and c) $n_y = 1$ ($N_3 = 1$). Dashed arrowed lines show the primitive translation vectors of the resulting superstructure. Here, we choose $\mathbf{e}_2 = (1, 0, 0)$, $\mathbf{e}_1 = (0, 0, 1)$, notice that the coordinate frame for the spin is rotated with respect to spatial frame (Axis x for the spin is the direction perpendicular to the plane and y is in plane axis perpendicular to the magnetic field.); d) Lines of the constant spin flux $\vec{\Phi}(\mathbf{r}) \cdot \mathbf{e}_1$ (dashed lines) from Eq. (3.4b), $\alpha = 0$ ($N_1 = 1$). Those lines can be also thought of as the spin current lines.

The dominant term in the free energy,

$$\mathbb{F}_\circ = \frac{1}{8} \left\{ \rho_K(r_0) \text{Tr} \left(\partial_\nu \hat{Q} \right)^2 + \frac{1}{4} [\rho_s(r_0) - \rho_K(r_0)] \left[-i \text{Tr} \hat{S}_z \hat{Q} \partial_\nu \hat{Q} \right]^2 \right\} \quad (4.4a)$$

[new notation is defined in Eq. (4.1)] has the symmetry which is higher than the symmetry of the original problem, see Eq. (2.12). Hereinafter, we will imply the summation over the repeating index $\nu = x, y$.

To facilitate the further analysis, we rewrite Eq. (4.4a) using parametrisation (3.2e)

$$\mathbb{F}_\circ = \frac{1}{4} \left\{ \rho_K(r_0) \text{Tr} \left(\partial_\nu \hat{V}^\dagger \partial_\nu \hat{V} \right) + \frac{1}{2} [\rho_s(r_0) - \rho_K(r_0)] \left[-i \text{Tr} \hat{V}^\dagger \partial_\nu \hat{V} \right]^2 \right\} \quad (4.4a')$$

where \hat{V} is a unitary 2×2 matrix. Further investigation of free energy (4.4a) is postponed until subsection IV A.

The remaining contributions, though may be small, are crucial because they remove artificial symmetries of the system. The following terms suppress $SU(2)$ rotations in the valley space:

$$\mathbb{F}_\perp = \frac{1}{8r_0^2} \sum_{\alpha=x,y,z} \eta_\alpha(r_0) \text{Tr} \hat{Q} \hat{\Lambda}_\alpha \hat{Q} \hat{\Lambda}_\alpha, \quad \eta_x = \eta_y = \eta_\perp. \quad (4.4b)$$

$$\mathbb{F}_\square = \frac{\kappa(r_0)}{16r_0^2} \sum_{\alpha,\beta=x,y} \text{Tr} \hat{Q} \hat{\Lambda}_\beta \hat{Q} \hat{\Lambda}_\beta \hat{Q} \hat{\Lambda}_\alpha \hat{Q} \hat{\Lambda}_\alpha, \quad (4.4c)$$

Finally, the term

$$\mathbb{F}_\triangleright = \frac{\zeta(r_0)}{4r_0^2} \text{Tr} \left[\left(\hat{Q} \hat{\Lambda}_+ \right)^6 + \left(\hat{Q} \hat{\Lambda}_- \right)^6 \right] \quad (4.4d)$$

generated by the Umklapp processes, reduces the $U(1)$ rotations in the valley space, to discrete rotations (2.5d).

A discussion of the role played by anisotropic terms (4.4b) – (4.4d) will be continued in subsection IV B.

A. Isotropic part of the action and topological defects

The sum over discrete topological defects can be replaced by a path integral over continuous variables - dual fields. Introduction of dual fields become more transparent when one uses the following parametrisation of the order parameter (3.2e):

$$V = e^{i\theta_s} g, \quad g = \begin{pmatrix} N_1 + iN_4 & iN_2 + N_3 \\ iN_2 - N_3 & N_1 - iN_4 \end{pmatrix} \quad (4.5)$$

where g is an $SU(2)$ matrix and $\sum_{i=1}^4 N_i^2 = 1$. Then free energy density (4.4a') acquires the form

$$\mathbb{F}_\circ = \frac{\rho_K}{2} \sum_{i=1}^4 (\partial_\nu N_i)^2 + \frac{\rho_s}{2} (\partial_\nu \theta_s)^2, \quad (4.4a'')$$

So it appears that the $U(1)$ and the $SU(2)$ sectors of the theory are decoupled. This decoupling, however, breaks down when one takes into account the topological defects. As we shall demonstrate, the non-Abelian sector changes the selection rules for the vortices winding numbers.

As usual for compact theories, the free energy density expression obtained in continuous limit has to be supplemented by topological defects to take into account

a behavior of the order parameter in the vicinity of some singular points \mathbf{r}_j , where it vanishes: $\hat{Q}^2(\mathbf{r}_j) = 0$; $\hat{V}(\mathbf{r}_j) \hat{V}^\dagger(\mathbf{r}_j) = 0$. The absolute value of the order parameter is established at the distances of the order of ξ_{MF} , see Eq. (4.3), and at large distances, the defect is characterized by a contour integral around it.

The topological defects are characterized by the winding number

$$q = \frac{i}{4\pi} \oint dx_\nu \text{Tr} (V^+ \partial_\nu V) \quad (4.6)$$

The most standard approach would be to keep the g matrix in Eq. (4.5) single-valued and non-singular and create 2π -vortex configuration in $U(1)$ field θ_s :

$$e^{i\theta_s} = \frac{(x-x_i) \pm i(y-y_i)}{\sqrt{(x-x_i)^2 + (y-y_i)^2}}; \quad (4.7)$$

$$\frac{1}{2\pi} \oint dx_\nu \partial_\nu \theta_s = \frac{i}{4\pi} \oint dx_\nu \text{Tr} (V^+ \partial_\nu V) = \pm 1,$$

If only such excitations were present, $U(1)$ and $SU(2)$ sectors would remain decoupled and the standard Berezinskii-Kosterlitz-Thouless transition^{12,13} would occur in the $U(1)$ sector.

There are, however, other configurations which are energetically more profitable than those of (4.7). Indeed, consider the configuration of the form

$$\hat{V}_{1/2} = e^{i\mathbf{n} \cdot \hat{\sigma}/2} \begin{pmatrix} \frac{(x-x_i) \pm i(y-y_i)}{\sqrt{(x-x_i)^2 + (y-y_i)^2}}; & 0 \\ 0; & 1 \end{pmatrix} e^{-i\mathbf{n} \cdot \hat{\sigma}/2}, \quad (4.8)$$

where $\mathbf{n}(\mathbf{r})$ is a smooth three-dimensional unit vector $\sum_{i=1}^3 n_i^2 = 1$, and $\hat{\sigma}_i$ are the Pauli matrices.

Re-writing Eq. (4.8) in the form of Eq. (4.5), we obtain instead of Eq. (4.7)

$$q = \frac{i}{4\pi} \oint dx_\nu \text{Tr} (V^+ \partial_\nu V) \pm \frac{1}{2}. \quad (4.9)$$

i.e. configuration (4.8) corresponds to a π or *half-vortex* in the $U(1)$ sector glued with a *half-vortex* in the $SU(2)$ -sector. Since the stiffness in the $SU(2)$ sector vanishes at large distances, the change of sign of g in large defects does not require energy. So in the absence of anisotropy the main effect of the $SU(2)$ sector is the change in selection rules of the vortices reflected in their topological invariant (4.6).

To anticipate a role of the vortex and half-vortex configurations in the thermodynamic properties of the system we evaluate their energies. Substituting configurations (4.7) and (4.8) into Eqs. (4.4a') or (4.4a''), we find

$$E_{1/2} = \left(\frac{1}{2} \right)^2 \pi (\rho_s + \rho_K) \ln \left(\frac{L}{\xi_{MF}} \right); \quad (4.10)$$

$$E_1 = \pi \rho_s \ln \left(\frac{L}{\xi_{MF}} \right);$$

where L is the system size. As $\rho_K \leq \rho_s$, one can see that the half-vortices are in fact the main configurations responsible for the disordering of the $U(1)$ sector, which we will in due course incorporate into the corresponding RG equations.

To treat the contributions of the topological configurations (4.7) and (4.9) systematically, we rewrite the partition function (4.2) (still neglecting the anisotropic parts) in the form

$$\begin{aligned} \mathcal{Z} &\propto \int \mathcal{D}\hat{V}\mathcal{D}\hat{h} \exp \left[-\frac{1}{T} \int d^2\mathbf{r} \mathbb{F} \left\{ \hat{V}, \hat{V}^\dagger, \hat{h} \right\} \right]; \\ \frac{\mathbb{F}}{T} &= \frac{1}{4} \text{Tr} \left\{ \frac{\rho_K}{T} \partial_x \hat{V}^\dagger \partial_x \hat{V} + \frac{T}{\rho_K} \left(\partial_x \hat{h} \right)^2 + 2\hat{V}^\dagger \partial_y \hat{V} \partial_x \hat{h} \right\} \\ &+ \frac{[\rho_s - \rho_K]}{8T} \left[-i \text{Tr} \hat{V}^\dagger \partial_x \hat{V} \right]^2 + \left[\frac{T}{8\rho_s} - \frac{T}{8\rho_K} \right] \left[\text{Tr} \partial_x \hat{h} \right]^2 \\ &- \frac{2\mu_1}{r_0^2} \cos 2\pi h_s - \frac{2\mu_{1/2}}{r_0^2} \frac{\sin \pi |\vec{h}|}{\pi |\vec{h}|} \cos \pi h_s; \\ \hat{V}\hat{V}^\dagger &= \mathbb{1}; \quad \hat{h} = \hat{h}^\dagger = h_s \mathbb{1}^s + \vec{h} \cdot \hat{\tau}^s \end{aligned} \quad (4.11)$$

where 2×2 matrix \hat{h} is the dual field, $\hat{\tau}_{x,y,z}^s$ are the Pauli matrices in the spin space, and $\mu_1, \mu_{1/2}$, are fugacities for the vortices and half-vortices respectively. Though it may appear that term Eq. (4.11) breaks the rotational symmetry, all the physical correlation functions calculated with using Eq. (4.11) are rotationally symmetric. Derivation of Eq. (4.11) is relegated to Appendix A

Summing up the leading logarithmic series within the first loop renormalization group scheme, we find the following equations for the corresponding fugacities:

$$\frac{d\mu_{1/2}}{d \ln r_0} = \left[2 - \left(\frac{1}{2^2} \right) \frac{\pi}{T} (\rho_K + \rho_s) \right] \mu_{1/2}. \quad (4.12a)$$

They are valid for $\mu_{1/2}, \mu \ll 1$ and also $\rho_K \gg T$.

The fugacity for the conventional vortices evolves as

$$\frac{d\mu_1}{d \ln r_0} = \left(2 - \frac{\pi \rho_s}{T} \right) \mu_1 \quad (4.12b)$$

for $\mu_1 \ll 1$. Equations (4.12) are analogous for the simple estimate of the energy of the defects (4.10), however, they allow for a renormalization of the stiffness ρ_s caused by the bound pairs of (half)vortices and (half)antivortices, and of the stiffness ρ_K caused by the bound pairs the half-vortices and anti-half-vortices as well as by thermal fluctuations of the order parameter. The latter renormalization, for $\mu_{1/2}, \mu \ll 1$ and $\rho_K \gg T$, can be represented in the form

$$\frac{d\rho_K}{d \ln r_0} = -\frac{T}{\pi} - \mu_{1/2}^2 \beta_K^{(1/2)}(\rho_K, \rho_s); \quad (4.13a)$$

$$\frac{d\rho_s}{d \ln r_0} = -\mu_{1/2}^2 \beta_s^{(1/2)}(\rho_K, \rho_s) - \mu_1^2 \beta_s^{(1)}(\rho_s). \quad (4.13b)$$

Functions β in Eqs. (4.13) are difficult to obtain explicitly for arbitrary stiffnesses. However, such forms will not be necessary for the further consideration.

As the initial fugacities of the half-vortices, $\mu_{1/2}$ are not much smaller than the fugacities for the vortices μ_1 , the latter ones being less relevant can be neglected in the description of the phase transition. In the limit of $\mu_{1/2} \ll 1$ one can also neglect the half-vortices in the renormalization of ρ_K . Then, from Eq. (4.13a) we obtain the following equations

$$\rho_K(r_0) = \frac{T}{\pi} \ln \frac{\xi_K}{r_0}; \quad \xi_K = \xi_{MF} \exp \left(\frac{\pi \rho(\xi_{MF})}{T} \right), \quad (4.14)$$

for $\xi_{MF} \lesssim r_0 \lesssim \xi_K$. At $r_0 \sim \xi_K$ the perturbative renormalization group is no longer valid, and the $SU(2)$ sector enters into the strongly disordered regime. Hence length ξ_K has a meaning of the correlation length of the order parameter.

At $r_0 \gg \xi_K$ the non-Abelian stiffness vanishes: $\rho_K \rightarrow 0$. We can then use Eq. (4.12a) to obtain the value of the Kosterlitz jump at the phase transition:

$$\frac{\pi \rho_s (T_{KT} - 0)}{T} = 2 * 2^2; \quad (4.15a)$$

This value is modified in comparison with the pure $U(1)$ model

$$\frac{\pi \rho_s (T_{KT} - 0)}{T} = 2; \quad (4.15b)$$

due to the presence of half-vortices and the $SU(2)$ sector being disordered.

Assuming that $\mu_{1/2}(\xi_{MF}) \ll 1$, we can also use Eq. (4.15a) to estimate T_{KT} :

$$\frac{\pi \rho_s (T_{KT})}{2T_{KT}} = 2^2 + \mathcal{O} [\mu_{1/2}(\xi_{MF})]; \quad (4.16)$$

In Sec. V we will use Eq. (4.16) to relate T_{KT} to mean-field transition temperature T_{MF} .

The main conclusions of these subsections are: (i) spin $U(1)$ and valley $SU(2)$ rotations are coupled to each other in the presence of *half-vortices*, and (ii) the $U(1)$ sector acquires the algebraic order at $T < T_{KT}$ whereas the isotropic version of the valley rotations always remain disordered.

The purpose of the next two subsections is to analyze how the disorder in the valley space is affected when the artificial symmetries are lifted by the leading anisotropies.

B. Effect of weak anisotropies.

Let us assume that the BKT transition in the $U(1)$ sector has already occurred so that the half-vortices are not relevant, and $SU(2)$ sector is decoupled. (This assumption will be lifted in Sec. IV C.) Then the thermal fluctuations lead to the renormalization of the anisotropies in the same fashion as the first term in the right-hand-side

of Eq. (4.13a). In the first loop approximation, we find

$$\begin{aligned}\frac{d\eta_\alpha}{d\ln r_0} &= \left[2 - \frac{2T}{\pi\rho_K}\right] \eta_\alpha; \\ \frac{d\kappa}{d\ln r_0} &= \left[2 - \frac{8T}{\pi\rho_K}\right] \kappa; \\ \frac{d\zeta}{d\ln r_0} &= \left[2 - \frac{12T}{\pi\rho_K}\right] \zeta;\end{aligned}\quad (4.17)$$

Solving Eq. (4.17) with the help of Eq. (4.14), we obtain

$$\begin{aligned}\eta_\alpha(r_0) &= \eta_\alpha(\xi_{MF}) \left(\frac{r_0}{\xi_{MF}}\right)^2 \left(\frac{\ln \frac{\xi_K}{r_0}}{\ln \frac{\xi_K}{\xi_{MF}}}\right)^2 \\ \kappa(r_0) &= \kappa(\xi_{MF}) \left(\frac{r_0}{\xi_{MF}}\right)^2 \left(\frac{\ln \frac{\xi_K}{r_0}}{\ln \frac{\xi_K}{\xi_{MF}}}\right)^8 \\ \zeta(r_0) &= \zeta(\xi_{MF}) \left(\frac{r_0}{\xi_{MF}}\right)^2 \left(\frac{\ln \frac{\xi_K}{r_0}}{\ln \frac{\xi_K}{\xi_{MF}}}\right)^{12}.\end{aligned}\quad (4.18)$$

These equations are valid for $r_0 \lesssim \xi_K$.

Thus, the effect of the anisotropies is determined by their value at distances of the order of ξ_K . If they are still small, i.e.

$$\begin{aligned}\eta_\alpha(\xi_{MF}) &\lesssim T \left(\frac{\xi_{MF}}{\xi_K}\right)^2 \left(\ln \frac{\xi_K}{\xi_{MF}}\right)^2; \\ \kappa(\xi_{MF}) &\lesssim T \left(\frac{\xi_{MF}}{\xi_K}\right)^2 \left(\ln \frac{\xi_K}{\xi_{MF}}\right)^8; \\ \zeta(\xi_{MF}) &\lesssim T \left(\frac{\xi_{MF}}{\xi_K}\right)^2 \left(\ln \frac{\xi_K}{\xi_{MF}}\right)^{12},\end{aligned}\quad (4.19)$$

then the $SU(2)$ sector remains disordered and the conclusions of the previous subsection remain qualitatively valid. If, however, one or several conditions (4.19) are violated, the anisotropies are important in determining the phase diagram of the system.

The phase diagram obviously depends on the relative values of the coupling constants η, κ, ζ and their signs. The latter are determined by the microscopic coupling constants (2.13) – (2.16), see also Sec. V. Since such couplings can not be established on a merely symmetry grounds, we will analyze the phase diagrams in the most possible general case and then construct the “physical” phase diagram in Sec. V E.

Let us assume

$$\begin{aligned}\bar{\eta}(\xi_{MF}) &\equiv [\eta_\alpha^2(\xi_{MF})]^{1/2} \gtrsim T \left(\frac{\xi_{MF}}{\xi_K}\right)^2 \ln^2 \frac{\xi_K}{\xi_{MF}}; \\ \kappa, \zeta &\ll \bar{\eta};\end{aligned}\quad (4.20)$$

Then, at the distance

$$R_* \simeq \xi_{MF} \left(\frac{T}{\bar{\eta}(\xi_{MF})} \ln^2 \frac{\xi_K}{\xi_{MF}}\right)^{1/2}\quad (4.21)$$

we have

$$\bar{\eta}(R_*) \simeq \rho_K(R_*),\quad (4.22)$$

so that the anisotropy becomes more important than the stiffness, and the perturbative treatment (4.17) is no longer valid.

Instead, one has to identify the remaining soft-modes still compatible with the anisotropy potential (4.4b) and consider the fluctuations for those modes only. To achieve this goal, let us re-write Eq. (4.4b) using the parametrization (4.5):

$$\mathbb{F}_\perp = \frac{1}{R_*^2} [(\eta_\perp + \eta_z) N_1^2 + (\eta_z - \eta_\perp) N_4^2],\quad (4.23)$$

and the isotropic part is given by Eq. (4.4a''), and $\sum_{i=1}^4 N_i^2 = 1$.

If there were no thermal fluctuations at all, the direction of the order parameter would be obtained by minimizing the expression (4.23) with the results summarized on Fig. 4.

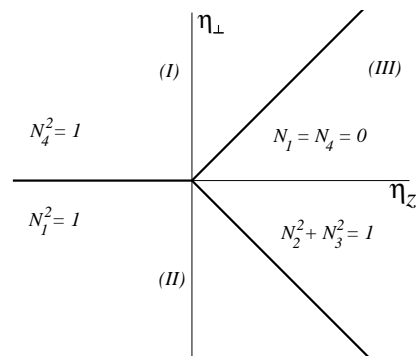


FIG. 4: Phase diagram in the absence of the thermal fluctuation. For the pictorial representation of the states in terms of physical spins see Fig. 3.

The regions (I) and (II) on Fig. 4, correspond to the Ising type anisotropy and the region (III) corresponds to the XY model. Hence deep inside the regions (I), (II) the system is ordered, whereas the region (III) is characterized by an algebraic order. At the lines separating those regions the system possesses extra degeneracies which will be analyzed separately.

1. Vicinity of the line $\eta_\perp = 0$, $\eta_z < 0$.

Near this line one can neglect the fluctuations of $N_{2,3}$ and consider $N_{1,4}$ only. Then, the relevant part of the free energy, see Eqs. (4.4a'') and (4.23), acquires the form

$$\mathbb{F}_{14} = \frac{\rho_K}{2} [(\partial_\nu N_1)^2 + (\partial_\nu N_4)^2] + \frac{\eta_\perp}{R_*^2} (N_1^2 - N_4^2),\quad (4.24)$$

with $N_{1,4}$ constrained by $N_1^2 + N_4^2 = 1$. Representing $N_1 = \cos \phi$, $N_4 = \sin \phi$ and introducing dual field θ to describe the vortices with a core size $\lesssim R_*$, we find

$$\begin{aligned} \mathcal{Z} &\propto \int \mathcal{D}\phi \mathcal{D}\theta \exp(-\mathbb{F}_{14}/T); \\ \frac{\mathbb{F}_{14}}{T} &= \frac{\rho_K}{2T} (\partial_x \phi)^2 + \frac{T}{2\rho_K} (\partial_x \theta)^2 + i\partial_x \theta \partial_y \phi \\ &+ \frac{\eta_\perp}{R_*^2 T} \cos 2\phi + \frac{\mu_{14}}{R_*^2} \cos(2\pi\theta), \end{aligned} \quad (4.25)$$

The derivation of Eq. (4.25) is completely analogous to the derivation of Eq. (4.11), see also Appendix. A.

The first loop scaling equations for the anisotropy η_\perp and the vortex fugacities μ_{14} are

$$\begin{aligned} \frac{d\mu_{14}}{d \ln r_0} &= \left(2 - \frac{\pi\rho_K}{T}\right) \mu_{14}; \\ \frac{d\eta_\perp}{d \ln r_0} &= \left(2 - \frac{T}{\pi\rho_K}\right) \eta_\perp. \end{aligned} \quad (4.26)$$

They have the obvious solutions

$$\begin{aligned} \mu_{14}(r_0) &= \mu_{14}(R_*) \left(\frac{R_*}{r_0}\right)^{\frac{\pi\rho_K - 2T}{T}}; \\ \eta_\perp(r_0) &= \eta_\perp(R_*) \left(\frac{R_*}{r_0}\right)^{\frac{T - 2\pi\rho_K}{\pi\rho_K}}. \end{aligned} \quad (4.27)$$

If $\eta_\perp(R_*) = 0$, the system undergoes Berezinskii-Kosterlitz-Thouless transition at $T_{BKT} = \pi\rho_K/2$; from the high temperature vortex-dominated disordered state to a phase with power law correlations.

At non-zero η_\perp the ordered phase has a finite correlation length since below $\pi\rho_K/2$ the anisotropy η_\perp is a relevant perturbation. Therefore, phase ϕ is locked and the system is ordered with a finite correlation length ξ_{14} determined by the condition $\eta_\perp(\xi_{14}) \simeq T$ so that

$$\xi_{14} \simeq R_* \left(\frac{T}{\eta_\perp(R_*)}\right)^{\frac{\pi\rho_K}{2\pi\rho_K - T}}. \quad (4.28)$$

From Eq. (4.28) one may conclude that the transition between phases (I) and (II) of Fig. 4 is a continuous one with smoothly varying correlation length exponent along the transition line. However, we will see shortly that this conclusion is an artifact of neglecting the higher order anisotropy (4.4c).

At temperatures above $\pi\rho_K/2$, both the anisotropy (order) and the vortices (disorder) are relevant. The corresponding operators compete with each other since θ and ϕ cannot be locked simultaneously. To estimate the location of the transition line and the length scale ξ_I at which criticality becomes important, we require

$$\frac{\eta_\perp(\xi_I)}{T} \simeq \mu_{14}(\xi_I) \simeq 1,$$

which yields, assuming as usual that $\mu_{14}(R_*) \ll 1$,

$$\begin{aligned} \xi_I &\simeq R_* \left(\frac{1}{\mu_{14}(R_*)}\right)^{\frac{T}{2T - \pi\rho_K}}; \\ \eta_c(\rho_K) &= T [\mu_{14}(R_*)]^{\frac{T}{\pi\rho_K} \frac{2\pi\rho_K - T}{2T - \pi\rho_K}} \end{aligned} \quad (4.29)$$

At distances larger than ξ_I , the anisotropy is the largest scale in the problem, so that N_1 (N_4) becomes massive and the vortices provide the possibility for N_4^2 (N_1^2) to change on the scale of the order of ξ_I . The resulting transition, therefore, involves only one soft mode and thus belongs to the Ising model universality class, see Appendix B, for more accurate calculation in the vicinity of $\pi\rho_K = T$. The corresponding correlation length ξ is, then, given by

$$\xi \simeq \xi_I \frac{\eta_\perp^c}{|\eta_\perp - \eta_\perp^c|}, \quad |\eta_\perp - \eta_\perp^c| \lesssim \eta_\perp^c. \quad (4.30)$$

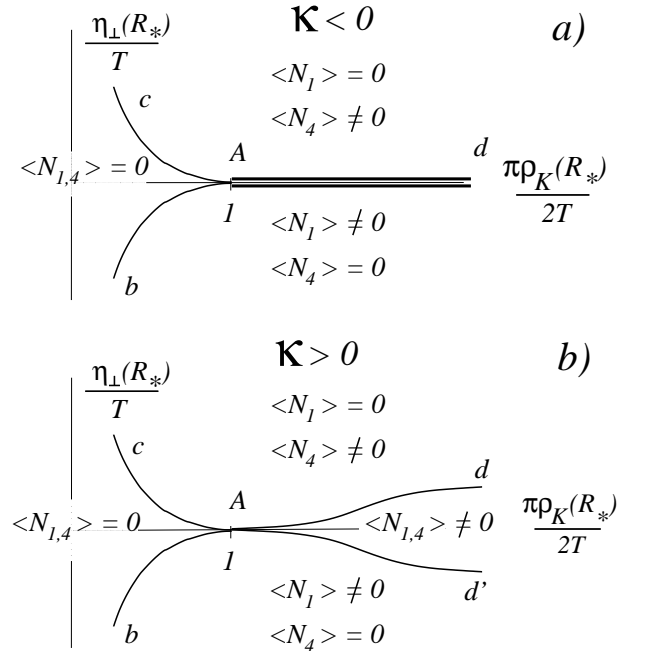


FIG. 5: Phase diagrams in the vicinity of the line $\eta_\perp = 0$, $\eta_z < 0$. Lines A – b and A – c are always of the Ising type. a) Line A – d is (weak) first order phase transition line at $\kappa < 0$. b) Lines A – d and A – d' are second order phase transitions (Ising type) at $\kappa > 0$. At $\kappa = 0$, the A – d line is a continuous phase transition with the varying indices given by Eq. (4.28).

So far we ignored the higher order anisotropy term. In fact, those terms are important only in the vicinity of (I)-(II) transition line, where they change the order of the phase transition.

To see this, we rewrite Eq. (4.4c) using parameterizations (3.2e) and (4.5):

$$\frac{\mathbb{F}_\square}{T} = \frac{\kappa(R_*)}{TR_*^2} \text{Re}(N_x + iN_y)^4 = \frac{\kappa(R_*)}{TR_*^2} \cos 4\phi. \quad (4.31)$$

Equation (4.31) should be added to Eq. (4.25).

The coupling in Eq. (4.31) is renormalised by thermal fluctuations. The first loop RG equation and its solution is given by

$$\begin{aligned} \frac{d\kappa}{d\ln r_0} &= \left(2 - \frac{4T}{\pi\rho_K}\right)\kappa; \\ \kappa(r_0) &= \kappa(R_*) \left(\frac{R_*}{r_0}\right)^{\frac{4T-2\pi\rho_K}{\pi\rho_K}}. \end{aligned} \quad (4.32)$$

At $\pi\rho_K > 2T$ the quartic anisotropy κ is a relevant perturbation, so that the phase ϕ becomes locked and the system is ordered in locally stable state even for $\eta_\perp = 0$, so that the correlation length ξ_{14} is always limited by $\tilde{\xi}_{14}$, that is found from the condition $\kappa(\tilde{\xi}_{14}) \simeq T$. It yields

$$\xi_{14} \lesssim \tilde{\xi}_{14} \simeq R_* \left(\frac{T}{|\kappa(R_*)|}\right)^{\frac{\pi\rho_K}{2\pi\rho_K-4T}}. \quad (4.33)$$

The length $\tilde{\xi}_{14}$ diverges when the approaching the multi-critical point $\pi\rho_K = 2T$, $\eta_\perp = 0$. At length scale large than $\tilde{\xi}_{14}$ the non-vanishing order parameter is found by minimisation of the expression

$$\frac{\tilde{\mathbb{F}}}{T} = \frac{\eta_\perp(\tilde{\xi}_{14})}{\tilde{\xi}_{14}^2 T} \cos 2\phi + \text{sgn}\kappa \cos 4\phi \quad (4.34)$$

with respect to ϕ which produces two second order (Ising type) phase transitions for $\kappa > 0$, and the first order phase transition for $\kappa < 0$ [in the former case $\tilde{\xi}_{14}$ serves as pre-factor for the diverging correlation length similarly to Eq. (4.30)].

At $\pi\rho_K < 2T$ the quartic anisotropy becomes irrelevant and we obtain from Eqs. (4.32) and (4.29)

$$\kappa(\xi_I) = \kappa(R_*) \left(\frac{1}{\mu_{14}}\right)^{\frac{2}{\pi\rho_K}} < T, \quad (4.35)$$

i.e. it can not affect the position and the universality class of the Ising phase transitions.

The resulting structure of the phase diagram in the vicinity of the line $\eta_\perp = 0$, $\eta_z < 0$ is summarised on Fig. 5.

2. Vicinity of the lines $\eta_z > 0$, $\eta_\perp = \pm\eta_z$.

In the vicinity of the line $\eta_z > 0$, $\eta_\perp = -\eta_z$ anisotropy (4.23) generates mass for the field N_4 so that the free energy for the remaining soft modes, see Eqs. (4.4a'') and (4.4d), is

$$\begin{aligned} \mathbb{F} &= \frac{\rho_K(R_*)}{2} \sum_{i=1}^3 (\partial_\nu N_i)^2 \\ &+ \frac{\Delta\eta(R_*)}{R_*^2} N_1^2 + \frac{\zeta(R_*)}{R_*^2} \text{Re}(N_2 + iN_3)^6; \\ N_1^2 + N_2^2 + N_3^2 &= 1; \quad \Delta\eta(R_*) \equiv \eta_z(R_*) + \eta_\perp(R_*), \end{aligned} \quad (4.36)$$

where length scale R_* and the coupling constants are defined in Eqs. (4.21), (4.14), and (4.18). The vicinity of the line $\eta_z > 0$, $\eta_\perp = \eta_z$ does not require a separate consideration as it is also described by the free energy density (4.36) after the replacement

$$N_1 \rightarrow N_4; \quad \eta_\perp(R_*) \rightarrow -\eta_\perp(R_*). \quad (4.37)$$

At $r_0 > R_*$, the scaling of the couplings in Eq. (4.36) is governed by the first loop renormalization group equations

$$\frac{d\rho_K}{d\ln r_0} = -\frac{T}{2\pi} \quad (4.38a)$$

$$\frac{d\Delta\eta}{d\ln r_0} = \left[2 - \frac{3T}{2\pi\rho_K}\right] \Delta\eta; \quad (4.38b)$$

$$\frac{d\zeta}{d\ln r_0} = \left[2 - \frac{21T}{2\pi\rho_K}\right] \zeta, \quad (4.38c)$$

where we neglect the effect of the anisotropies on the renormalization of the stiffness which, however, will be sufficient for our purposes.

The solution of Eq. (4.38a) is

$$\rho_K(r_0) = \frac{T}{2\pi} \ln \frac{\xi_H}{r_0}; \quad \xi_H = R_* \exp\left(\frac{2\pi\rho(R_*)}{T}\right), \quad (4.39a)$$

which is consistent with the well known fact that the classical $SU(2)/U(1)$ sigma model is always disordered by the thermal fluctuations with ξ_H being the correlation length for these fluctuations.

Anisotropies may lead to ordering. To estimate positions of the phase transition lines, we solve Eqs. (4.38b) and (4.38c) with the help of Eq. (4.39a) and find

$$\begin{aligned} \Delta\eta(r_0) &= \Delta\eta(R_*) \left(\frac{r_0}{R_*}\right)^2 \left(\frac{\ln \frac{\xi_H}{r_0}}{\ln \frac{\xi_H}{R_*}}\right)^3 \\ \zeta(r_0) &= \zeta(R_*) \left(\frac{r_0}{R_*}\right)^2 \left(\frac{\ln \frac{\xi_H}{r_0}}{\ln \frac{\xi_H}{R_*}}\right)^{21}. \end{aligned} \quad (4.39b)$$

First, let us neglect the hexadic anisotropy, $\zeta = 0$. Then, the anisotropy is important if $|\Delta\eta(r_0 \simeq 2\xi_H)| > T$. Equations (4.39b) and (4.39a) give us approximate positions of the phase transition lines

$$\begin{aligned} \frac{\Delta\eta_\perp(R_*)}{T} &= \left(\alpha_\perp \frac{2\pi\rho_K(R_*)}{T}\right)^3 \exp\left(-\frac{4\pi\rho_K(R_*)}{T}\right); \\ \frac{\Delta\eta_I(R_*)}{T} &= -\left(\alpha_I \frac{2\pi\rho_K(R_*)}{T}\right)^3 \exp\left(-\frac{4\pi\rho_K(R_*)}{T}\right), \end{aligned} \quad (4.40)$$

shown on Fig. 6. The numerical pre-factors $\alpha_{I,\perp}$ of order of unity can not be obtained within a perturbative RG scheme.

Line $\Delta\eta_I$ corresponds to the second order phase transition from the disordered phase to the phase characterised

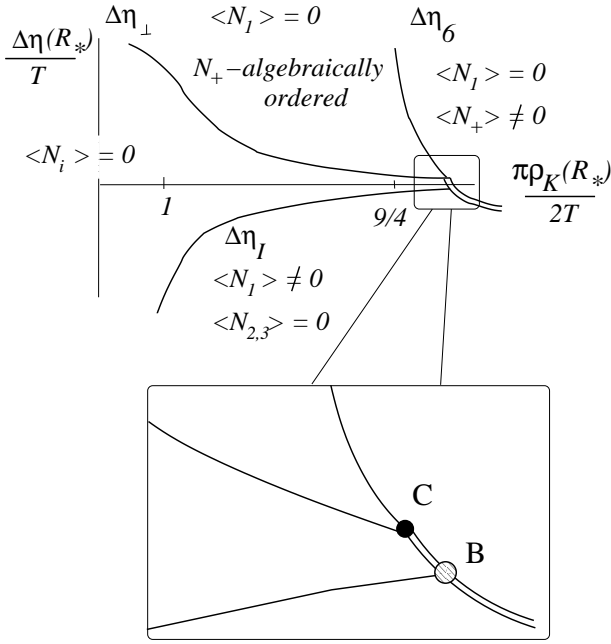


FIG. 6: Phase diagrams in the vicinity of the line $\Delta\eta = \eta_z + \eta_\perp = 0$, $\eta_z > 0$. Here $N_+ = N_2 + iN_3$. Lines $\Delta\eta_{\perp,6}$ are the Berezinskii-Kosterlitz-Thouless phase transitions. Line η_I is the Ising type phase transition. Double line is the first order phase transition. Point C is the bi-critical point and point B is the critical end point.

by $\langle N_1 \rangle \neq 0$. This phase transition belongs to the universality class of the two dimensional Ising model. Additional hexadical anisotropy, (finite but small ζ) can not affect this transition.

Line $\Delta\eta_\perp$ corresponds to the phase transition from the disordered phase to the phase characterised by algebraic correlations for $N_{2,3}$, i.e. to the Berezinskii-Kosterlitz-Thouless transition. Contrary to the Ising transition, the hexadical term may cause a further ordering and an additional Berezinskii-Kosterlitz-Thouless type transition between the algebraically ordered to the long-range ordered phase.

To describe those two transitions, we put $N_1 = 0$ in Eq. (4.36), introduce the field ϕ , so that $N_2 = \cos\phi$, $N_3 = \sin\phi$, and the dual field θ to describe the vortices.

The singular part of the partition function is given by

$$\begin{aligned} \mathcal{Z} &\propto \int \mathcal{D}\phi \mathcal{D}\theta \exp(-\mathbb{F}_{23}/T); \\ \frac{\mathbb{F}_{23}}{T} &= \frac{\rho_K}{2T} (\partial_x \phi)^2 + \frac{T}{2\rho_K} (\partial_x \theta)^2 + i\partial_x \theta \partial_y \phi \\ &+ \frac{\zeta}{R_\perp^2 T} \cos 6\phi + \frac{\mu_{23}}{R_\perp^2} \cos(2\pi\theta), \end{aligned} \quad (4.41)$$

where the coupling constant are described by Eqs. (4.14) and (4.39b) and $R_\perp < R_H$ found from the requirement

$\rho_K(R_\perp) \simeq \Delta\eta(R_\perp)$. This yields

$$\frac{R_\perp}{\xi_H} \ln \frac{R_\perp}{\xi_H} = \left(\frac{\Delta\eta_\perp(R_*)}{\alpha_\perp^3 \Delta\eta(R_*)} \right)^{1/2}. \quad (4.42)$$

Once again, the scaling of the vortex fugacity, μ_{23} , and of the hexadical anisotropy, ζ , can be determined from the first loop renormalization group equations

$$\frac{d\mu_{23}}{d \ln r_0} = \left[2 - \frac{\pi\rho_K}{T} \right] \mu_{23}; \quad (4.43a)$$

$$\frac{d\zeta}{d \ln r_0} = \left[2 - \frac{9T}{\pi\rho_K} \right] \zeta. \quad (4.43b)$$

In the limit of $\mu_{23}, \zeta \ll 1$, Eqs. (4.43) enable us to refine the definitions of α_\perp (requiring $\pi\rho_K(R_\perp) = 2T$) and to find the boundary of the ordered phase $\eta_6(R_*)$ (requiring $\pi\rho_K(R_\perp) = 9T/2$). With the help of Eqs. (4.42) and (4.39a), we find

$$\begin{aligned} \alpha_\perp &\approx \frac{e^2}{2^{4/3}} \approx 2.9; \\ \eta_6 &\approx \left(\frac{4e^9}{9e^4} \right)^2 \eta_\perp \approx 4.3 * 10^3 \eta_\perp, \end{aligned} \quad (4.44)$$

i.e. even though the boundaries of two phases have the same functional form, they are very well separated due to the numerical reasons.

In the previous discussion, we implied that $\zeta(R_\perp) \ll 1$. This condition is clearly violated on the lines η_6 , η_\perp , η_I if $\pi\rho_K/T \rightarrow \infty$, see the last of Eqs. (4.39b). Large power of the logarithm allows one to use the saddle point expression and we obtain from condition $\zeta(R_\perp) \gtrsim 1$:

$$\frac{\pi\rho(R_*)}{2T} > \frac{21}{8} + \left(\frac{21}{32} \ln \frac{T}{\zeta(R_*)} \right)^{1/2}. \quad (4.45)$$

At larger stiffness, the phase transition occurs by the locking of the order parameter due to the hexadical term and the fluctuations become unimportant. Minimising the potential part of free energy (4.36), we obtain a first order phase transition at $\eta(R_*) \simeq \zeta(R_*)$.

The only way of connecting the critical lines on the phase diagram, allowed by the symmetries of the system is shown in the inset of Fig. 6.

C. Effect of strong anisotropies.

In Sec. IV B we assumed that $U(1)$ sector was ordered and the half-vortices were not important in ordering the $SU(2)$ sector. It was justified by the assumption of the weak enough anisotropy so that the parameter $\bar{\eta}$, see Eq. (4.20), is constrained by $\bar{\eta}(\xi_{MF}) \ll T$. In this case, the renormalization of the stiffness ρ_K is so strong that $\rho_K(R_*) \ll \rho_s$ [see Eq. (4.21)] and separation of the scale was justified. We will see, however, in Sec. V D that for some ranges of the in-plane magnetic field the opposite

limits of the strong anisotropies, $\bar{\eta}(\xi_{MF}) \gtrsim T$ are more relevant.

In this case the logarithmic renormalization of the stiffness ρ_K , see Eq. (4.13a), and of the anisotropy parameters, see Eq. (4.17) are no longer strong and one has to investigate the soft modes in Eq. (4.23) already on the scale of the order of ξ_{MF} . Similarly to the approach of IVB only the lines of extra degeneracies requires further investigation. The difference is that $U(1)$ sector and the *half-vortex* configurations have to be taken into account. To simplify further manipulations, we introduce the parameter

$$\gamma \equiv \frac{\rho_K(R_*)}{\rho_s(R_*)} < 1. \quad (4.46)$$

All the results of the previous subsection correspond to the limiting case $\gamma \rightarrow 0$.

1. The vicinity of line $\eta_\perp = 0$, $\eta_z < 0$.

Let us generalise Eq. (4.25) by including the half-vortices. Substituting parametrisation (4.5) with $N_{2,3} = 0$, $N_1 = \cos \phi$, $N_4 = \sin \phi$ into Eq. (4.11), representing $2\hat{h} = \text{diag} [\theta + h_s; \theta - h_s]$, we obtain

$$\begin{aligned} \mathcal{Z} &\propto \int \mathcal{D}\phi \mathcal{D}\theta \mathcal{D}\phi_s \mathcal{D}\theta_s \exp(-\mathbb{F}_{14}/T); \\ \frac{\mathbb{F}_{14}}{T} &= \left[\frac{\rho_K}{2T} (\partial_x \phi)^2 + \frac{T}{2\rho_K} (\partial_x \theta)^2 + i\partial_x \theta \partial_y \phi \right. \\ &\quad \left. + \frac{\mu_{14}}{R_*^2} \cos(2\pi\theta) + \frac{\eta_\perp}{R_*^2 T} \cos 2\phi \right] + \\ &\quad + \left[\frac{\rho_K}{2\gamma T} (\partial_x \theta_s)^2 + \frac{T\gamma}{2\rho_K} (\partial_x h_s)^2 + i\partial_x h_s \partial_y \theta_s \right. \\ &\quad \left. + \frac{\mu_1}{R_*^2} \cos(2\pi h_s) \right] + \frac{\mu_{1/2}}{R_*^2} \cos(\pi h_s) \cos(\pi\theta) \end{aligned} \quad (4.47)$$

[to obtain μ_{14} term by generating vortices is completely analogous to Eq. (4.25)]. Here γ is given by (4.46), μ_{14} is a fugacity for creation of a vortex in ϕ field (we will call them “ $N_1 - N_4$ vortices”), the vortices in θ_s field [we will call them “vortices in the $U(1)$ sector”] are governed by the fugacity μ_1 , and $\mu_{1/2}$ is the fugacity for the half-vortices.

The first loop RG equations are analogous to Eqs. (4.12), and (4.26):

$$\begin{aligned} \frac{d\mu_{1/2}}{d \ln r_0} &= \left[2 - \frac{\pi\rho_K}{4T} \left(\frac{1+\gamma}{\gamma} \right) \right] \mu_{1/2}; \\ \frac{d\mu_{14}}{d \ln r_0} &= \left(2 - \frac{\pi\rho_K}{T} \right) \mu_{14}; \\ \frac{d\mu_1}{d \ln r_0} &= \left(2 - \frac{\pi\rho_K}{\gamma T} \right) \mu_1; \\ \frac{d\eta_\perp}{d \ln r_0} &= \left(2 - \frac{T}{\pi\rho_K} \right) \eta_\perp; \end{aligned} \quad (4.48)$$

We will see, that $\gamma = 1/4$ is a special point where the $N_1 - N_4$ vortices have the same scaling dimension as the half-vortices for the disordered valley sector. Another special point is $\gamma = 1/3$ where the half-vortices become more relevant in the disordering the $N_1 - N_4$ sector than the simple vortices.

The phase diagram for $\gamma < 1/4$ is shown on Fig. 7. The physics in the vicinity of the multi-critical point A is still determined by $N_1 - N_4$ vortices whereas the half-vortices are irrelevant in this region. Inside the $N_1 - N_4$ disordered region any deformation in ϕ causes only a finite energy,

$$\langle \cos \pi\theta \rangle \neq 0.$$

Therefore, the half-vortices in $U(1)$ sector are allowed and the condition (4.15a) determines the value of the Kosterlitz jump. In fact, $\cos \pi\theta$ is proportional to the disorder operator μ of the Ising model, see Ref. 23. We will use this analogy shortly.

On the other hand, deep in the ordered sector, the half-vortices are confined and the disordering the $U(1)$ sector occurs due to the vortices and, thus, the Kosterlitz jump is determined by Eq. (4.15b).

Only vicinities of the tricritical points $D_{1,2}$, $D'_{1,2}$ on the Fig. 7 a) deserve a special consideration. In their vicinity μ_1 term in (4.47) is irrelevant and μ_{14} and η_\perp terms conspire to produce an Ising critical point. Therefore at $\mu_{1/2} = 0$ we have two decoupled critical theories: the Ising one described by ϕ, θ fields and the $U(1)$ model described by (θ_s, h_s) fields. At the Ising model critical point the operator $\cos \theta$ behaves as the disorder parameter field of the Ising model and has scaling dimension $1/8$. Hence the corresponding RG equation for $\mu_{1/2}$ is

$$\frac{d\mu_{1/2}}{d \ln r_0} = \left[2 - \frac{1}{8} - \frac{\pi\rho_s(r_0)}{4T} \right] \mu_{1/2}, \quad (4.49)$$

where we restored ρ_s using Eq. (4.46).

The scale invariance requirement for the fugacity $\mu_{1/2}$ gives the stiffness at the multi-critical points $D_{1,2}$

$$\frac{\pi\rho_s^c(r_0 \rightarrow \infty)}{2T_c} = \frac{15}{4} < 4. \quad (4.50)$$

If $\rho_s < \rho_s^c$, the half-vortex fugacity $\mu_{1/2}$ grows according to Eq. (4.49) as

$$\frac{\mu_{1/2}(r_0)}{\mu_{1/2}(R_*)} = \left(\frac{r_0}{R_*} \right)^{\frac{15(\rho_s^c - \rho_s)}{8\rho_s^c}} \quad (4.51)$$

The growth (4.51) has to be stopped at the correlation length of the Ising transition

$$\xi_I \simeq \frac{\eta_\perp^c}{|\eta_\perp - \eta_\perp^c|}.$$

At the lengths larger than ξ^I the Ising model becomes ordered, so the half-vortices are confined. However, their fusion produces usual vortices with the fugacity

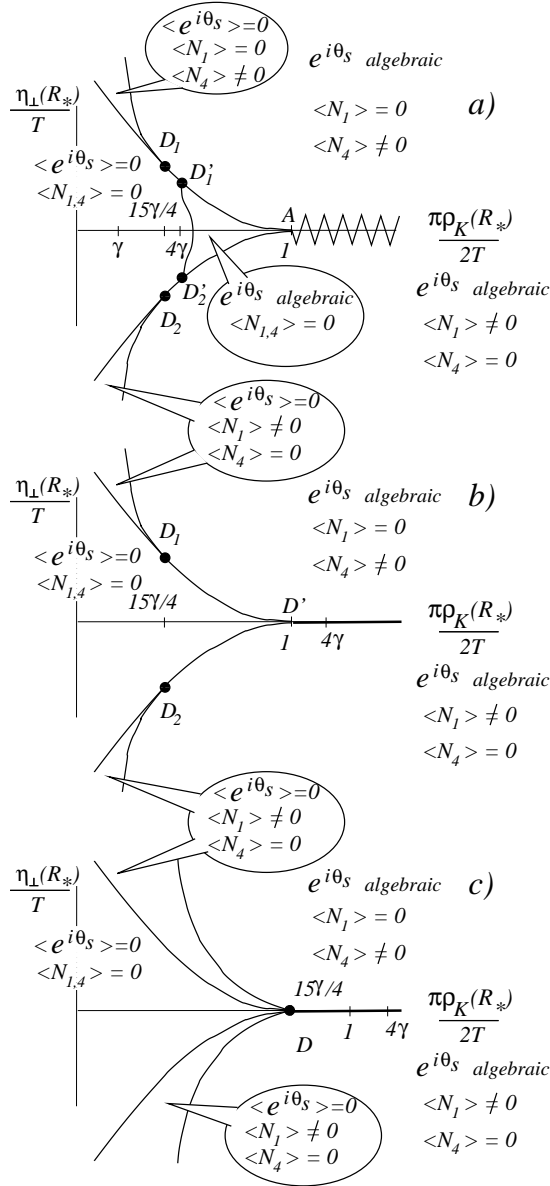


FIG. 7: The phase diagram in the vicinity of the line $\eta_{\perp} = 0$ for different values of γ ; a) $\gamma < 1/4$; Zigzag line denotes either the first order phase transition or pair of the Ising transition, see Fig. 5. The asymptotics of the Berezinskii-Kosterlitz-Thouless lines are given by Eqs. (4.52) and (4.55) for points $D_{1,2}$ and $D'_{1,2}$ respectively. b) $1/4 < \gamma < 4/15$; The asymptotics of the Berezinskii-Kosterlitz-Thouless lines are given by Eqs. (4.52) for points $D_{1,2}$. c) $1/3 < \gamma < 1/4$. The difference between the slopes of the Ising and the Berezinskii-Kosterlitz-Thouless near multi-critical point B is given by Eqs. (4.52). Finite κ leads to the modification of the multi-critical point B .

$\mu_1 \simeq \mu_{1/2}^2(\xi_I)$. The requirement for the resulting parameters of the remaining $U(1)$ theory to be on the line of the Berezinskii-Kosterlitz-Thouless transition leads to

the estimate $\mu^{1/2}(\xi_I) \simeq 1$ or, see also Fig. 5 a),

$$\ln \frac{\eta_c}{\eta_{\perp}^{KT} - \eta_{\perp}^c} = \frac{8\rho_s^c}{15(\rho_s^c - \rho_s)} + \mathcal{O}(1). \quad (4.52)$$

For the spin stiffnesses, in the interval

$$\rho_s^c < \rho_s < \rho_s^{c,2}, \quad \frac{\pi\rho_s^{c,2}}{2\pi} = 4, \quad (4.53)$$

the fugacity for the half-vortices (4.51) vanishes at $r_0 \rightarrow \infty$. If one tries to deviate from the line $\eta = \eta_c$ towards the ordered side, those half-vortices fuse into vortices which are also irrelevant.

Let us now consider the deviation from the tricritical point towards the disordered side of the Ising sector. In this region $\cos\theta$ can be replaced by its average. As we have mentioned above, near the Ising model critical line $\cos\theta \sim \mu$ (the disorder operator of the Ising model). Hence we find

$$\cos\pi\theta \cos\pi h_s \rightarrow |\eta_{\perp} - \eta_c^{\perp}|^{1/8} \cos\pi h_s. \quad (4.54)$$

The latter operator is irrelevant in the region (4.53) as well. Therefore, the line $\eta = \eta_c$, $\rho_s^c < \rho_s < \rho_s^{c,2}$, is the transition line both for the valley and the spin sectors²².

At $\rho > \rho_s^{c,2}$, the half-vortices in the limit of the zero-fugacity $\mu_{1/2}$ become irrelevant and $U(1)$ sector is algebraically ordered. The correction to vertical line can be evaluated using

$$\rho_s - \rho_s^{c,2} \simeq \mu_{1/2}(\xi_I) \propto |\eta_{\perp} - \eta_c^{\perp}|^{1/8}. \quad (4.55)$$

This estimate is valid near points $D'_{1,2}$.

Case $\gamma > 1/4$ needs further investigation as the critical points $D'_{1,2}$ crosses the point A , see Fig. 7 b,c). For simplicity, we will neglect the quartic anisotropies: $\kappa = 0$.

Let us first consider $1/4 < \gamma < 4/15$. If $\eta_{\perp}(R_*) = 0$, the system undergoes the Berezinskii-Kosterlitz-Thouless transition and $\pi\rho_K/2T = 1$ where $N_1 - N_4$ vortices become relevant, $\langle \cos 2\pi\theta \rangle \neq 0$. At the same time $\langle \cos\pi\theta \rangle \neq 0$ and the remaining factor of the half-vortex operator becomes relevant, with the dimensionality $\pi\rho_K/(4\gamma T)$. As the result, the $U(1)$ sector also becomes disordered.

Initial steps in the consideration of $\eta_{\perp} \neq 0$ are the same as in the derivation of Eqs. (4.29) and (4.30), and we obtain two lines of the Ising phase transitions. The scaling of the half-vortex fugacity on the Ising line is still governed by Eq. (4.49) so that the conclusions of Eqs. (4.50) and (4.52) remain intact, see Fig. 7 b).

The peculiarity of $4/15 < \gamma < 1/3$ regime is that the half-vortex operator becomes relevant on the whole Ising line, whereas it is still irrelevant in the ordered region. As the result the points $D_{1,2}$ on Fig. 7 b) collapse, see Fig. 7 c). The positions of the Berezinskii-Kosterlitz-Thouless lines still can be estimated using Eqs. (4.50) and (4.51).

The most delicate case which we were not able to solve is $\gamma > 1/3$. In this situation the *half-vortices* are always more relevant than the vortices and the transitions

both in $U(1)$ and in $N_1 - N_4$ sectors occur due to the half-vortices. The corresponding free energy obtained by keeping only half-vortices in Eq. (4.47) is

$$\begin{aligned} \frac{\mathbb{F}_{14}}{T} &= \frac{\rho_K}{2T} (\partial_x \phi)^2 + \frac{T}{2\rho_K} (\partial_x \theta)^2 + i \partial_x \theta \partial_y \phi \\ &+ \frac{\rho_K}{2\gamma T} (\partial_x \theta_s)^2 + \frac{T\gamma}{2\rho_K} (\partial_x h_s)^2 + i \partial_x h_s \partial_y \theta_s \quad (4.56) \\ &+ \frac{\mu_{1/2}}{R_*^2} \cos(\pi h_s) \cos(\pi \theta) + \frac{\eta_\perp}{R_*^2 T} \cos 2\phi. \end{aligned}$$

We do not know the critical property of this model of this model in the strong coupling line.

2. The vicinity of lines $\eta_z > 0$, $\eta_\perp = \pm \eta_z$.

The analysis of those lines relies on the material of Secs. IV C 1 and IV B 2. Near the line $\eta_z > 0$, $\Delta\eta = |\eta_\perp| - \eta_z \ll \eta_z$, we have to generalise Eq. (4.36) [see also Eq. (4.37)] to include $U(1)$ sector. In this subsection we also neglect the hexadic anisotropy $\zeta = 0$. The resulting theory is obtained from Eq. (4.11) by putting extra constraint on the unitary matrix \hat{V}

$$\begin{aligned} \hat{V}^\dagger &= -\hat{V}, \quad \eta_\perp < 0; \\ \hat{V}^\dagger &= \hat{\tau}_y \hat{V} \hat{\tau}_y, \quad \eta_\perp > 0. \end{aligned} \quad (4.57)$$

One case case is mapped to the other by the substitution $\hat{V} \rightarrow i \hat{\tau}_y \hat{V}$ and therefore only one of them has to be studied.

The line $\Delta\eta_I$, see Eq. (4.40) is of the Ising type and all the analysis of Eqs. (4.49) – (4.55) is still valid.

What remains is the vicinity of the Berezinskii-Kosterlitz-Thouless transition line $\Delta\eta_\perp$, see Fig. 8. The theory describing phase transition in this case is, compare with Eq. (4.41), can be written in terms of dual fields only,

$$\begin{aligned} Z &\propto \int \mathcal{D}h_s \mathcal{D}\theta \exp(-\mathbb{F}_{23}/T); \\ \frac{\mathbb{F}_{23}}{T} &= \frac{T}{2\rho_K(R_{**})} (\partial_\mu \theta)^2 + \frac{T}{2\rho_s} (\partial_\mu h_s)^2 \quad (4.58) \\ &+ \frac{\mu_{23}(\Delta\eta)}{R_{**}^2} \cos 2\pi\theta + \frac{\mu_{1/2}(\Delta\eta)}{R_{**}^2} \cos \pi h_s \cos \pi \theta, \end{aligned}$$

where $\rho_s \gg \rho_K(R_{**})$ because of the strong logarithmic renormalization at distances where the valley sector is almost isotropic. It has a sequence of two phase transitions shown on Fig. 8 by lines $\Delta\eta_\perp$ and $\Delta\eta_{1/2}$.

D. Resulting phase diagram.

In Secs. IV B, IV C, we analysed of the vicinities of the degeneracies point and the vicinities of the degeneracies lines of Fig. 4. The results of this analysis enable us to

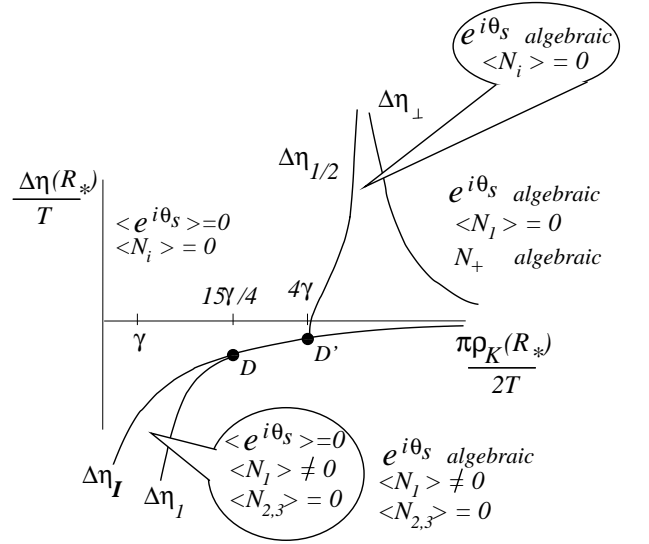


FIG. 8: Phase diagrams in the vicinity of the line $\Delta\eta = \eta_z + \eta_\perp \ll \eta_z$, $\eta_z > 0$ for finite value of γ , see Eq. (4.46), and in the absence of the hexadic anisotropies, $\zeta = 0$. Here $N_+ = N_2 + iN_3$. Lines $\Delta\eta_{\perp,1,1/2}$ are the Berezinskii-Kosterlitz-Thouless phase transitions. Line η_I is the Ising type phase transition. The asymptotics of the lines $\Delta\eta_{1,1/2}$ are given by Eqs. (4.52) and (4.55) for points D and D' respectively (those points are equivalent to the multi-critical points of Fig. 7 a) with the same notation. The transitions across the lines $\Delta\eta_{1,\perp}$ are controlled by the unbinding of the vortices, and $\Delta\eta_{1/2}$ is governed by the half-vortices.

construct the phase diagrams in terms in the plane defined by anisotropies $(\eta_z(R_*), \eta_\perp(R_*))$, see also Eqs. (4.20) and (4.21). Indeed, there can be no other singularities than those we have already considered, because for all the other regions of the phase diagrams the $SU(2)$ sector is massive due to the anisotropies. Therefore, the character of the singularities along the phase transition line remain the same.

Bearing this in mind and expressing $\rho_K(R_*)$ in terms of anisotropies using Eq. (4.22), we construct the “global” phase diagram shown on Fig. 9. The relation of this phase diagram to the physical coordinates B, T will be found in Sec. V E after the microscopic theory for the parameters of Landau free energy is built.

V. LOGARITHMIC RENORMALIZATIONS AND MEAN FIELD TRANSITION

The specifics of the problem in hand that it has three different interval of the logarithmic reormalizations: (i) energies larger than Zeeman splitting; (ii) energies larger than temperature but smaller than Zeeman splitting; (iii) classical renormalizations considered in the previous Section. As those renormalization are contributed by different degrees of freedoms they have to be considered separately. The result will be the microscopic expres-

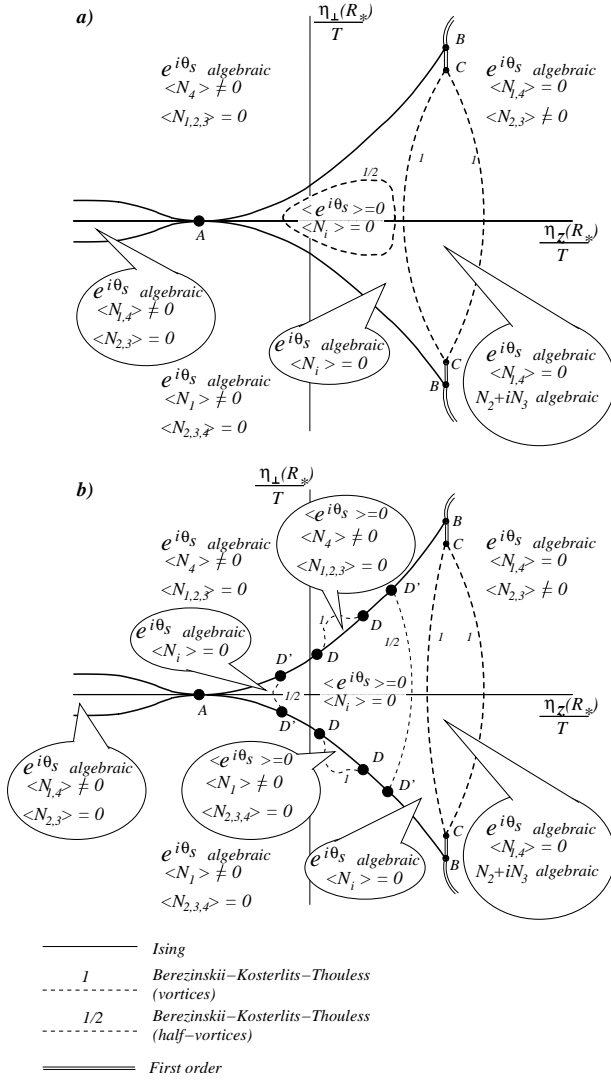


FIG. 9: The overall phase diagram for (a) decoupled valley and spin sectors, $\gamma \rightarrow 0$; and (b) for $\gamma < 1/4$. The positive quartic anisotropy, $\kappa > 0$ is assumed. The more detailed behaviour near the multi-critical points A, B, C, D are shown in more details near Figs. 5–8. The notation for those points here is consistent with that for Figs. 5–9.

sions for the coupling constants in the free energy which will enable us to construct the physical phase diagram in Sec. V E.

A. Logarithmic renormalizations at energies larger than Zeeman splitting.

At such energies the Zeeman splitting is not important and can be considered perturbatively if necessary. We will also assume that the short range interaction and umklapp terms are not strong enough to lead to any reconstruction in the state of the system at high energies, so they also can be considered within the perturbation theory, leading to a simple modification of the coupling

constants which are not well-known anyway.

The only terms which require the special attention are those related to the long-range Coulomb interaction. Indeed, a simple dimensional analysis of the Hamiltonian (2.10) – (2.11) points to logarithmic divergences in the simple perturbation theory (first identified in Ref. 6 for the three-dimensional gapless semiconductors).

As usual, a summation of the leading logarithmic divergences is performed within the renormalization group scheme. However, the loop expansion would not be suitable for the description of the graphene as the dimensionless interaction strength $e^2/v(r_c)$ is not small at distances $r_c \simeq a$.

Instead, the expansion in terms of N – the number of independent fermion species entering the Hamiltonian (2.10) – (2.11) will be used. For the problem at hand, we have the valley and spin degeneracies so that $N = 4$. The results, which will be obtained, indicate, that $1/N$ corrections are quite small for $N = 4$, so that $1/N$ expansion seems to be a reasonable approximation.

To make the calculations compact, we will utilise the standard imaginary time diagrammatic technique¹⁴. Analytic expressions for the corresponding lines are given on Fig. 10.

$$\begin{aligned}
 \text{---} \xrightarrow{\epsilon, \vec{k}} &= -\hat{G}(\epsilon, \vec{k}) \\
 \bigcirc &= -v(r_c) \vec{k} \hat{\Sigma}; \quad \hat{G} = \frac{1}{i\epsilon + \bigcirc} \\
 \square &= -\mathcal{B} \hat{S}_z; \\
 \text{~~~~~} \omega, \vec{q} &= -\frac{2\pi e^2}{|\vec{q}|} \\
 \hexagon &= \frac{1}{2} \lambda_w(r_c) v(r_c) r_c \hat{\Lambda}_z \left[(k_x + ik_y)^2 (\hat{\Sigma}_x + i\hat{\Sigma}_y) + h.c. \right]; \\
 \text{---} \bullet \text{---} &= -r_c v(r_c) \sum_{\alpha, \beta=x,y,z} F_{\alpha\beta}(r_c) \hat{\Sigma}_\alpha \hat{\Lambda}_\beta \otimes \hat{\Sigma}_\alpha \hat{\Lambda}_\beta \\
 &\quad - r_c v(r_c) \sum_{\alpha=x,y,z} \left[J_\alpha^\Sigma(r_c) \hat{\Sigma}_\alpha \otimes \hat{\Sigma}_\alpha + J_\alpha^\Lambda(r_c) \hat{\Lambda}_\alpha \otimes \hat{\Lambda}_\alpha \right] \\
 \text{---} \bullet \text{---} &= r_c^3 v(r_c) \sum_{\alpha, \beta, \gamma=x,y,z} \left[\mathcal{F}_{\alpha\beta\gamma}(r_c) \hat{\Sigma}_\alpha \hat{\Lambda}_+ \otimes \hat{\Sigma}_\beta \hat{\Lambda}_+ \otimes \hat{\Sigma}_\gamma \hat{\Lambda}_+ + h.c. \right]
 \end{aligned}$$

FIG. 10: Basic elements for the diagrammatic calculation for Hamiltonian (2.9)–(2.17), at distances $r_c \lesssim R_B \equiv v(R_B)/\mathcal{B}$.

Performing the renormalization group procedure, we change the smallest spatial scale in the problem from $r_c^<$ to the exponentially larger scale $r_c^>$. It amounts to taking into account all the diagrams where the momenta q going through the Coulomb interaction propagator, belong to the region $1/r_c^> < |q| < 1/r_c^<$. This cut-off procedure, does not violate the gauge invariance or other symmetries

of the problem. Then, we rescale fermionic fields as $\psi \rightarrow (1 + \delta Z/2)\psi$, $\bar{\psi} \rightarrow (1 + \delta Z/2)\bar{\psi}$ in order to keep the term $\bar{\psi}\partial_\tau\psi$ intact³.

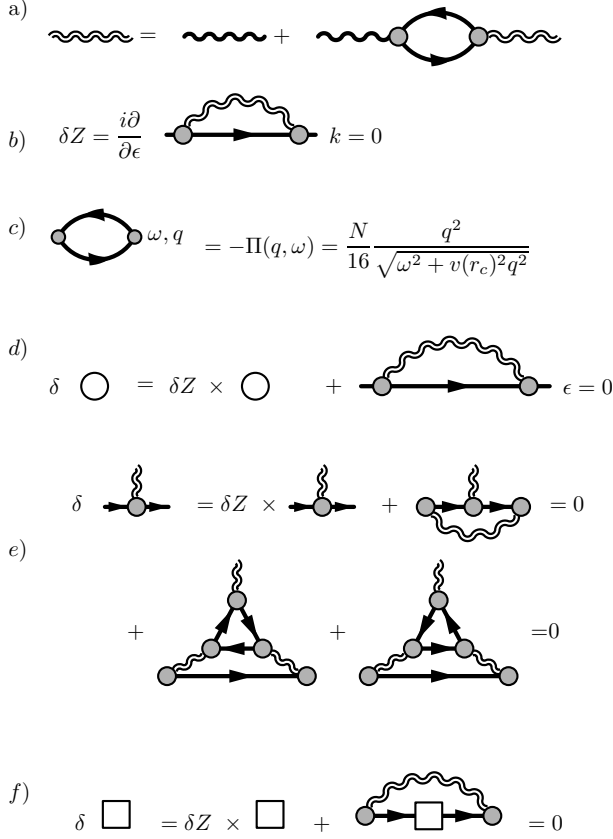


FIG. 11: Diagrammatic representation for the leading in $1/N$ renormalization of the parameters of the high-symmetric part of the Hamiltonian, see Eq. (2.10). All the basic elements are defined on Fig. 10. The integration over the momentum q going through the wiggly line is restricted by $1/r_c^> < |q| < 1/r_c^<$.

For the high-symmetry part of the Hamiltonian, see Eqs. (2.10) and (2.11), the only coupling which renormalises is the velocity $v(r_c)$. This renormalization is a consequence of non-Lorentz-invariance of the Coulomb interaction.

Introducing the dimensionless interaction strength

$$g(r_c) = \frac{\pi e^2 N}{8v(r_c)}, \quad (5.1)$$

³ In this scheme the scalar vertex and the Zeeman splitting term are not renormalised also, as a consequence of the gauge invariance. This can be checked by explicit calculation of the diagrams of Fig. 11 e,f).

and calculating the diagrams of Fig. 11 d), we obtain

$$\frac{d \ln g}{d \ln r_c} = -\frac{8}{\pi^2 N} f_v(g), \quad (5.2)$$

where dimensionless function f_v is given by

$$f_v(g) = 1 - \frac{\pi}{2g} + \begin{cases} \frac{\arccos g}{g\sqrt{1-g^2}}, & g \leq 1; \\ \frac{\operatorname{arccosh} g}{g\sqrt{g^2-1}}, & g \geq 1. \end{cases} \quad (5.3)$$

It is easy to see that the function $f_v(g)$ is monotonously increasing and analytic for all $g > 0$, see Fig. 12. The asymptotic behaviour of this function is

$$f_v(g) \approx \begin{cases} \frac{\pi g}{4} - \frac{2g^2}{3} + \mathcal{O}(g^3), & g \ll 1; \\ 1 - \frac{\pi}{2g} + \frac{\ln 2g}{g^2} + \mathcal{O}\left(\frac{1}{g^4}\right), & g \gg 1. \end{cases} \quad (5.3')$$

Equations (5.2) – (5.3) were first obtained in Ref. 7 for $N = 1$ where they are not applicable beyond the first term in the expansion (5.3') for $g \ll 1$. The validity of those formulas for $N \gg 1$ was pointed out in Ref. 8, but the numerical coefficients here are different from the latter reference.

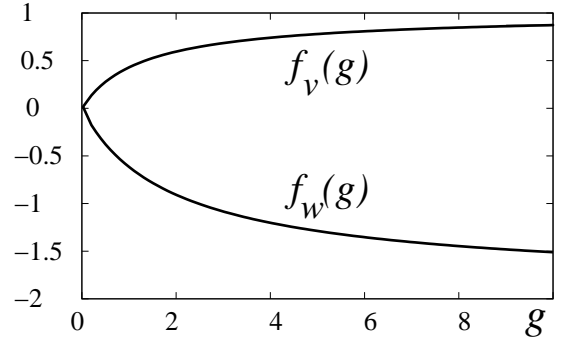


FIG. 12: Plots of functions $f_v(g)$ and $f_w(g)$ entering into renormalization group equations.

Solution of Eq. (5.2) with the help of the asymptotics (5.3') yields

$$g\left(\frac{r_c}{\mathcal{R}}\right) \approx \begin{cases} \left[\frac{2}{N\pi} \ln\left(\frac{r_c}{\mathcal{R}}\right) + 1 \right]^{-1}, & r_c \gtrsim \mathcal{R}; \\ \left(\frac{\mathcal{R}}{r_c}\right)^{\frac{8}{\pi^2 N}} \approx \left(\frac{\mathcal{R}}{r_c}\right)^{0.20}, & a \ll r_c \lesssim \mathcal{R}; \end{cases} \quad (5.4)$$

where \mathcal{R} is the only relevant spatial scale generated by interaction. This scale can be estimated as

$$\ln \frac{\mathcal{R}}{a} \simeq \begin{cases} \frac{\pi^2 N}{8} \ln g(a); & g(a) \gtrsim 1 \\ -\frac{\pi N}{2g(a)}; & g(a) \lesssim 1. \end{cases} \quad (5.5)$$

where a is the scale of the order of the lattice constant at which the continuous description becomes applicable.

For the graphene sheets, the reported velocity, see e.g. Ref. 17, is $v(a) \simeq 10^8 \text{ cm/s}$, we estimate $g \simeq 2 \div 4$ (uncertainty is associated with the dielectric properties of the substrate as well as uncertainty of linear scale at which the velocity is measured) and we find from Eq. (5.5)

$$\mathcal{R} \simeq 10^2 \div 10^3 a \gg a. \quad (5.6)$$

For all the further consideration we assume that the relation $\mathcal{R} \gg a$ is fulfilled.

The Coulomb interaction strongly affects the scaling of the low-symmetry terms of the Hamiltonian. Let us start from the trigonal warping term (2.13). Calculating diagrams shown in Fig. 13a, we find

$$\frac{d \ln \lambda_w}{d \ln r_c} = -1 + \frac{4}{\pi^2 N} f_w(g); \quad (5.7)$$

where negative monotonous analytic function

$$f_w(g) = -\frac{28}{15} + \frac{13\pi}{8g} + \frac{10}{g^2} - \frac{11\pi}{2g^3} - \frac{6}{g^4} + \frac{3\pi}{g^5} + \left(-\frac{4}{g} + \frac{7}{g^3} - \frac{3}{g^5} \right) \times \begin{cases} \frac{2 \arccos g}{\sqrt{1-g^2}}, & g \leq 1; \\ \frac{2 \operatorname{arccosh} g}{\sqrt{g^2-1}}, & g \geq 1; \end{cases} \quad (5.8)$$

is also plotted on Fig. 12.

The asymptotic behaviour of this function is

$$f_w \approx \begin{cases} -\frac{5\pi g}{16} + \frac{64g^2}{105} + \mathcal{O}(g^3), & g \ll 1; \\ -\frac{28}{15} + \frac{13\pi}{8g} + \frac{10 - 8 \ln 2g}{g^2} + \mathcal{O}\left(\frac{1}{g^3}\right), & g \gg 1. \end{cases} \quad (5.8')$$

Solution of Eq. (5.7) with the help of Eq. (5.8') yields

$$\frac{\lambda_w(r_c)}{\lambda_w(\mathcal{R})} \approx \begin{cases} \left(\frac{\mathcal{R}}{r_c} \right) \left[\frac{2}{N\pi} \ln \left(\frac{r_c}{\mathcal{R}} \right) + 1 \right]^{-5/8}, & r_c \gtrsim \mathcal{R}; \\ \left(\frac{\mathcal{R}}{r_c} \right)^{1 + \frac{112}{5\pi^2 N}} \approx \left(\frac{\mathcal{R}}{r_c} \right)^{1.57}, & a \ll r_c \lesssim \mathcal{R}; \end{cases} \quad (5.9)$$

where

$$\lambda_w(\mathcal{R}) \simeq \lambda_w(a) \left(\frac{a}{\mathcal{R}} \right)^{1.57} \simeq 10^{-3} \div 10^{-5}. \quad (5.10)$$

Thus, we see that the Coulomb interaction tends to suppress drastically the warping term making the energy surfaces more and more isotropic¹⁵.

On the other hand, the Coulomb interaction leads to the enhancement on the short-range interaction terms in

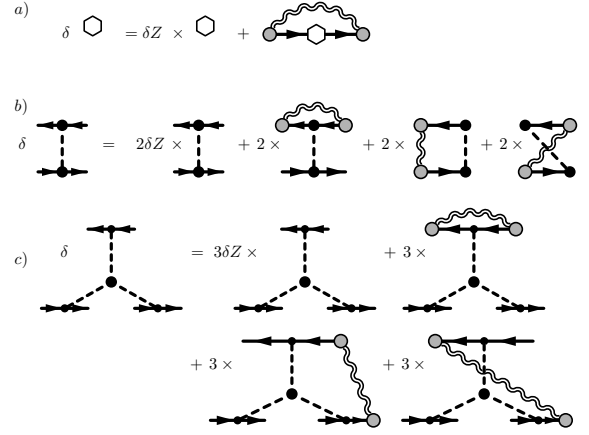


FIG. 13: Diagrammatic representation for the leading in $1/N$ renormalization of the parameters of the low-symmetric part of the Hamiltonian, see Eqs. (2.13), (2.14) and (2.16). All the basic elements are defined on Figs. 10, 11. The integration over the momentum q going through the wiggly line is restricted by $1/r_c^> < |q| < 1/r_c^<$.

the Hamiltonian (2.14). Calculating diagrams of Fig. 13 b) we find⁴

$$\begin{aligned} \frac{d \ln F_+^{z,\perp}}{d \ln r_c} &= \frac{d \ln J_+^{\Sigma,\Lambda}}{d \ln r_c} = \frac{d \ln J_+^\Lambda}{d \ln r_c} = -1; \\ \frac{d \ln F_-^{z,\perp}}{d \ln r_c} &= \frac{d \ln J_-^\Sigma}{d \ln r_c} = -1 + \frac{40}{\pi^2 N} f_v(g), \end{aligned} \quad (5.11)$$

where function $f_v(g)$ is defined in Eq. (5.3).

Equations (5.11) can be easily solved with the help of Eq. (5.2) and we find

$$\frac{F_+^{z,\perp}(r_c)}{F_+^{z,\perp}(a)} = \frac{J_+^{\Sigma,\Lambda}(r_c)}{J_+^{\Sigma,\Lambda}(a)} = \frac{J_+^\Lambda(r_c)}{J_+^\Lambda(a)} = \frac{a}{r_c}; \quad (5.12a)$$

$$\frac{F_-^{z,\perp}(r_c)}{F_-^{z,\perp}(a)} = \frac{J_-^\Sigma(r_c)}{J_-^\Sigma(a)} = \frac{a}{r_c} \left(\frac{g(a)}{g(r_c)} \right)^5. \quad (5.12b)$$

Couplings in the Eq. (5.12a) are irrelevant. The interactions in Eq. (5.12b) are strongly enhanced by the long-range Coulomb interaction. This enhancement becomes especially pronounced at intermediate distances $r_c \lesssim \mathcal{R}$. Using Eq. (5.4) we find

$$\frac{F_-^{z,\perp}(r_c)}{F_-^{z,\perp}(a)} = \frac{J_-^\Sigma(r_c)}{J_-^\Sigma(a)} \approx \left(\frac{r_c}{a} \right)^{\frac{40}{\pi^2 N} - 1} \approx \left(\frac{r_c}{a} \right)^{0.01},$$

⁴ Notice that the “mean-field analysis” of Ref. 5 of the excitonic instabilities at zero magnetic field corresponds to accounting of only the third diagram in the right-hand-side of Fig. 13 b) and thus is false even within $1/N$ approximation.

i.e. naively dimensionally irrelevant couplings become weakly relevant. Though, such small value of indices is clearly beyond the accuracy of the $1/N$ approximation for $N = 4$, this formula indicates, however, that the effect of the short range interaction lowering the symmetry of the system is much stronger than it was thought before. Whether or not this enhancement may lead to instability at zero magnetic field requires further improvement of the renormalization group scheme, which is beyond the scope of the present paper. Here, we simply note that at large distances. $g \rightarrow 1/\ln(r_c)$, see Eq. (5.4), so that the coupling of Eq. (5.12b) becomes irrelevant again. It indicates that at zero magnetic field the excitonic instability can occur only as a first order phase transition. In all subsequent consideration, we will assume that such transition does not occur. This assumption is in accord with all the experimental findings accumulated so far.

For the further use, let us recast the answer (5.12) for the most important constants, in the form similar to (5.9). Because of estimate (5.6), the second digits in the exponents are not observable and will be omitted:

$$F_{\pm}^{z,\perp}(r_c) \approx \begin{cases} F_{\pm}^{z,\perp}(\mathcal{R}); & r_c \lesssim \mathcal{R}; \\ F_{\pm}^{z,\perp}(\mathcal{R}) \frac{\mathcal{R}}{r_c} \left[\frac{2}{N\pi} \ln\left(\frac{r_c}{\mathcal{R}}\right) + 1 \right]^5; & r_c \gtrsim \mathcal{R}; \end{cases}$$

$$F_{\pm}^{z,\perp}(\mathcal{R}) \approx F_{\pm}^{z,\perp}(a) \simeq 1. \quad (5.13)$$

Finally, the Umklapp terms are also enhanced by the interaction. Calculating the contributions shown on Fig. 13 b), we obtain the renormalization group equations

$$\frac{d \ln \mathcal{F}_+}{d \ln r_c} = -3; \quad (5.14)$$

$$\frac{d \ln \mathcal{F}_-}{d \ln r_c} = -3 + \frac{64}{\pi^2 N} f_v(g).$$

Similarly to the (5.12), the solution of Eq. (5.14) is

$$\frac{\mathcal{F}_+(r_c)}{\mathcal{F}_+(a)} = \left(\frac{a}{r_c}\right)^3; \quad \frac{\mathcal{F}_+(r_c)}{\mathcal{F}_+(a)} = \left(\frac{a}{r_c}\right)^3 \left(\frac{g(a)}{g(r_c)}\right)^8. \quad (5.15)$$

In particular, at the intermediate distances $r_c \lesssim \mathcal{R}$, we find

$$\frac{\mathcal{F}_+(r_c)}{\mathcal{F}_+(a)} \approx \left(\frac{a}{r_c}\right)^{3 - \frac{64}{\pi^2 N}} \approx \left(\frac{a}{r_c}\right)^{1.4},$$

i.e. the three particle Umklapp interaction remain irrelevant though it is strongly enhanced by the Coulomb interaction.

To conclude this subsection we notice that the short range interaction terms are vital in the consideration of the QHE ferromagnets^{18,19} and the effect of warping on the weak localization was considered in Ref. 20. The results of this subsection indicates that the estimates done in those works are hardly reliable.

B. Logarithmic renormalizations at energies smaller than Zeeman splitting: separation of the electron-hole and the Cooper channels.

In the previous subsection we considered the Zeeman splitting as a perturbation. This is legitimate to do up to the spatial scale $r_c < R_B$, where the length R_B is found from the equation

$$v \left(\frac{R_B}{\mathcal{R}} \right) = \mathcal{B} R_B. \quad (5.16)$$

The scale dependent velocity v is determined from Eqs. (5.1) and (5.2) and we highlighted that this dependence may include only one spatial scale \mathcal{R} . To solve Eq. (5.16) and facilitate further discussion, we introduce the natural scale for the Zeeman splitting, \mathcal{B}_0 , according to

$$\mathcal{B}_0 = \frac{v(r_c = \mathcal{R})}{\mathcal{R}}, \quad (5.17)$$

rough estimate for \mathcal{B}_0 is $\mathcal{B}_0 \simeq 10 \div 10^2 K$. Then the solution of Eq. (5.16) takes the universal form

$$R_B = \mathcal{R} f_B \left(\frac{B}{B_0} \right) \quad (5.18)$$

where the function $f_B(x)$ is the solution of the equation

$$v[f_B(x)] = xv(1)$$

$$f_B(x) \approx 1/x^{1.25}; \quad x \gtrsim 1;$$

$$f_B(x) \approx \frac{2}{N\pi x} \ln\left(\frac{1}{x}\right) + \frac{1}{x}; \quad x \lesssim 1; \quad (5.19)$$

At $r_c > R_B$, Zeeman splitting freezes some electronic degrees of freedom, and, on the other hand, gives rise to the finite density of state for the other ones, see Fig. 2 b).

To make use of such separation, we will include the Zeeman splitting in the denominator of the Green function and decompose the result as

$$\hat{G} = \frac{1}{i\epsilon - v(R_B) \vec{k} \hat{\Sigma} - \mathcal{B} \hat{S}_z} = \hat{G} + \delta \hat{G};$$

$$\hat{G} = \hat{\mathcal{P}}(\vec{n}) \frac{1}{i\epsilon - \xi \hat{S}_z}; \quad \delta \hat{G} = \left(\mathbb{1} - \hat{\mathcal{P}}(\vec{n}) \right) \frac{1}{i\epsilon + (\xi - 2\mathcal{B}) \hat{S}_z};$$

$$\xi \equiv \mathcal{B} - v(R_B) |\vec{k}|; \quad \vec{n} = \frac{\vec{k}}{|k|}, \quad (5.20)$$

where

$$\hat{\mathcal{P}} \equiv \frac{1}{2} \left(1 - \vec{n} \cdot \hat{\Sigma} \hat{S}_z \right); \quad \hat{\mathcal{P}}^2 = \hat{\mathcal{P}}; \quad (5.21)$$

is the projection operator to the branches of the electron spectrum which may produce excitations with the energies smaller than \mathcal{B} .

The $\delta\mathcal{G}$ component of the Green function (5.20) does not have a resonant denominator and may be neglected. For the logarithmically divergent contributions only $\xi \lesssim \mathcal{B}$ are important so that the integration over the momentum can be replaced by

$$\int \frac{d^2k}{(2\pi)^2} \cdots \rightarrow \int \frac{d\vec{n}}{2\pi} \int_{-\mathcal{B}}^{\mathcal{B}} \frac{d\xi}{2\pi v^2(R_B)} \cdots \quad (5.22)$$

Usual calculation of the second order correction to the interaction vertex shown on Fig. 14 a,b) reveals two logarithmically divergent contributions, which can be readily identified as electron-hole (a) and Cooper (b) channels. It is worthwhile to emphasise that those contributions are associated with the presence of the Fermi surface, and have the structure very different from the high-energy logarithmic terms of the previous subsection.

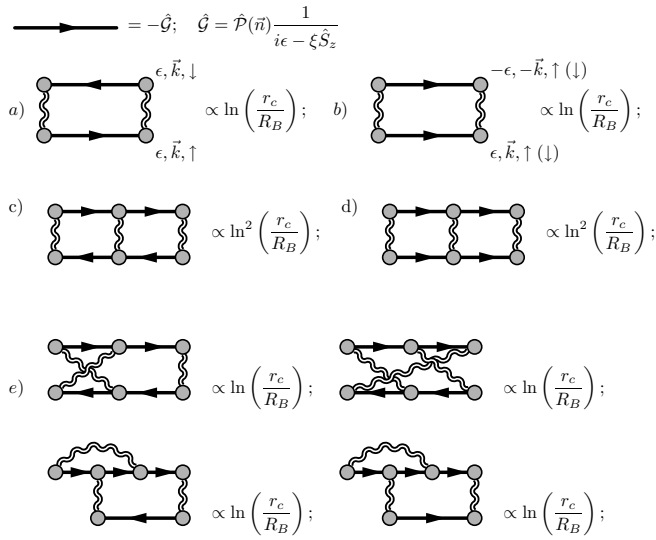


FIG. 14: Leading (a-d) and sub-leading (e) logarithmic divergences at $r_c > R_B$. Series (a,c) corresponds to the excitonic instability¹¹ in the electron-hole channel studied in the present series. The interaction in the Cooper channel (b,d) is repulsive and, therefore, renormalises to zero.

To collect the leading logarithmic divergences, we look at the third order diagram, and find that only those corresponding to the ladder series, see Fig. 14 b,d) are proportional to the second power of the logarithm. The sub-leading terms, see Fig. 14 e), can be combined as a perturbative (in $1/N$, or the interaction strength) renormalization of the coefficients in the second order diagram and, therefore, can be neglected.

Finally, it is easy to check that the signs of the diagrams Fig. 14 a) and c) are the same, whereas, the signs of the diagrams Fig. 14 b) and d) are different from each other. The latter corresponds to the repulsive interaction in the Cooper channel, which, thus renormalises to zero. The former one describes the attractive interaction of electron and hole and leads to the excitonic instability.

Therefore, the only relevant diagrammatic series is the ladder series in the electron-hole channel, which should

be summed up in all orders of the perturbation theory. The fact, that the logarithmic divergence occurs only in one channel justifies the mean-field approximation which will be employed in the next subsection.

C. Mean field transition.

After the leading divergent series is identified, it can be summed within the standard mean field approximation¹⁴, shown on Fig. 15a-c). Simple examination of the momentum q and frequencies ω transferred through the interaction wiggly line shows that all the momenta $q < \frac{2}{R_B}$ contribute almost equally into the formation of the order parameter, whereas the approximation $\omega \approx 0$ is valid with the logarithmic accuracy. The finite order parameter Δ changes the polarisation operator only for small $q \simeq \Delta/v(R_B) \ll \frac{1}{R_B}$. This modification may produce effect only of the order of Δ^2/\mathcal{B}^2 and it will be neglected, see Fig. 15 c-d).¹⁶

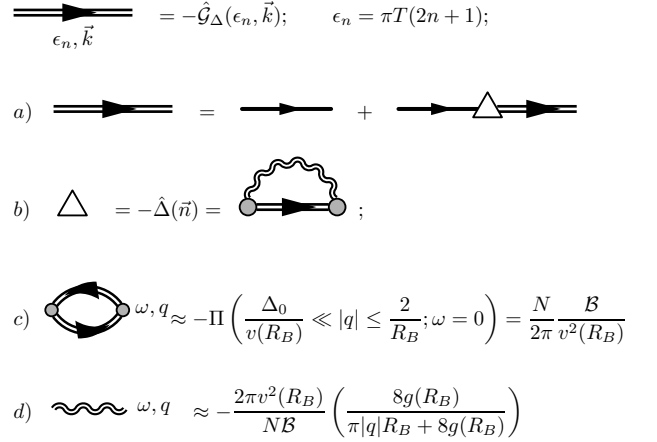


FIG. 15: Mean-field equations corresponding to the summation of the most divergent series, Fig. 14a), c).

The resulting mean field equations are obtained from Fig. 15 a-b) with the interaction propagator Fig. 15 c) using the approximation $|\vec{p}_1 - \vec{p}| \approx 2/R_B \sin \frac{1}{2} \widehat{\vec{n}}; \vec{n}_1$, valid once again with the logarithmic accuracy, and the integration rule (5.22). It results in

$$\hat{\Delta}(\vec{n}) = T \sum_{\epsilon_n = \pi T(2n+1)} \int \frac{dn_1}{2\pi} V(\widehat{\vec{n}} : \vec{n}_1) \times \hat{\mathcal{P}}(\vec{n}_1) \int_{-\mathcal{B}}^{\mathcal{B}} \frac{\mathcal{B}d\xi}{2\pi v^2(R_B)} \frac{i\epsilon_n - \xi \hat{S}_z + \Delta(\vec{n}_1)}{\epsilon_n^2 + \xi^2 + \hat{\mathcal{P}}(\vec{n}_1) \Delta(\vec{n}_1)^2} \quad (5.23)$$

where

$$V(\alpha) = \frac{2\pi v^2(R_B)}{N\mathcal{B}} \left(\frac{8g}{2\pi \sin \frac{|\alpha|}{2} + 8g} \right); \quad V_n \equiv \int_{-\pi}^{\pi} \frac{d\alpha}{2\pi} V(\alpha) \cos n\alpha. \quad (5.24)$$

Substituting $\hat{\Delta}(\vec{n})$ of the form

$$\hat{\Delta}(\vec{n}) = \hat{S}_x \hat{\Sigma}_z \left\{ \Delta_0(T) \hat{\mathcal{P}}(\vec{n}) + \Delta_1(T) \left[\mathbb{1} - \hat{\mathcal{P}}(\vec{n}) \right] \right\} \quad (5.25)$$

into Eq. (5.23), we find

$$\Delta_1(T) = \frac{V_1 - V_0}{V_1 + V_0} \Delta_0(T),$$

and the self-consistency relation involving $\Delta_0(T)$ only. At $T = 0$ the gap is given by

$$1 = \frac{(V_0 + V_1) \mathcal{B}}{4\pi v^2 (R_B)} \ln \frac{2\mathcal{B}}{\Delta_0}, \quad (5.26)$$

where the constants $V_{0,1}$ are given by Eq. (5.24).

Substituting Eq. (5.24) into Eq. (5.26), we obtain after the integration

$$\Delta_0(T = 0) = 2\mathcal{B} \exp \left(- \frac{2N}{f_{\Delta} \left(\frac{\pi}{4g(R_B)} \right)} \right), \quad (5.27)$$

where $f_{\Delta}(x) < 1$ is a dimensionless function of the scale dependent interaction strength (5.1), and R_B is defined by Eq. (5.16).

The explicit expression for this function is

$$f_{\Delta}(x) = \begin{cases} \frac{4}{\pi} \left[\frac{\sqrt{x^2 - 1}}{x^2} \operatorname{arccosh} x - \frac{1}{x} + \frac{\pi}{2x^2} \right], & x \geq 1 \\ \frac{4}{\pi} \left[-\frac{\sqrt{1 - x^2}}{x^2} \arccos x - \frac{1}{x} + \frac{\pi}{2x^2} \right], & x \leq 1 \end{cases} \quad (5.28)$$

and its asymptotic behaviour is given by

$$f_{\Delta}(x) \approx \begin{cases} 1 - \frac{4x}{3\pi} + \frac{x^2}{4} + \mathcal{O}(x^3), & x \ll 1 \\ \frac{4}{\pi x} \ln \frac{2x}{e} + \frac{2}{x^2} + \mathcal{O}\left(\frac{1}{x^3}\right), & x \gg 1 \end{cases}. \quad (5.28')$$

To write down the explicit expression for the zero-temperature gap, we use the scale of the magnetic field introduced in Eq. (5.17). If the magnetic field is weak, $\mathcal{B} \ll \mathcal{B}_0$, then $R_B \gg \mathcal{R}$, and the effective interaction is also weak, $g(R_B) \ll 1$. Using asymptotics Eqs. (5.4) and (5.28') in Eq. (5.27), we find

$$\Delta_0(T = 0) \approx 2\mathcal{B} \exp \left(- \frac{\pi \left[\ln \frac{\mathcal{B}_0}{\mathcal{B}} + \frac{N\pi}{2} \right]}{4 \ln \left[\ln \frac{\mathcal{B}_0}{\mathcal{B}} + \frac{N\pi}{2} \right]} \right). \quad (5.29a)$$

For the strong magnetic field, $\mathcal{B} \gg \mathcal{B}_0$, the result reads

$$\Delta_0(T = 0) \approx 2\mathcal{B} \exp \left\{ -2N \left[1 + \frac{1}{3} \left(\frac{\mathcal{B}_0}{\mathcal{B}} \right)^{\frac{8}{\pi^2 N}} \right] \right\}, \quad (5.29b)$$

i.e. the dependence slowly approaches the linear function.

To complete this subsection, we consider the effect of finite temperature. As for the usual BCS mean field, Eq. (5.23) gives the temperature dependence of the width of the mean-field gap $\Delta_0(T)$ which contains the scale $\Delta_0(0)$ only:

$$\ln \frac{T_{MF}}{T} + \sum_{n=0}^{\infty} \left[\frac{1}{\sqrt{\left(n + \frac{1}{2}\right)^2 + \frac{\Delta_0(T)^2}{4\pi^2 T^2}}} - \frac{1}{n + \frac{1}{2}} \right] = 0, \quad (5.30)$$

where T_c is related to $\Delta_0(0)$ by the usual weak coupling BCS relation

$$T_{MF} = \pi e^{-\mathbb{C}} \Delta_0(0) \approx 1.76 \Delta_0(0). \quad (5.31)$$

and \mathbb{C} is the Euler constant.

Equations (5.31) and (5.30) enable us to estimate the upper bound for the mean field crossover temperature. For $N = 4$ we find

$$T_{MF} \lesssim 10^{-3} \mathcal{B}, \quad (5.32)$$

where \mathcal{B} is the Zeeman splitting. As the electron g -factor in graphene equals to 2, we estimate for the parallel magnetic field $B \simeq 40T$, $T_{MF} \simeq 60mK$, which does not seem to be non-realistic. The other experimental realization could be putting the appropriate insulating ferromagnet on the top of the graphene film, so that the Zeeman splitting is caused by the corresponding exchange fields. The effective Zeeman splitting in this case may reach thousands of Kelvin- s^{21} .

In the vicinity of the mean-field crossover $T_c - T \ll T_c$, we obtain from Eq. (5.30)

$$\Delta_0(T)^2 = \frac{8\pi^2}{7\zeta(3)} T_c (T - T_c) \approx 9.38 T_{MF} (T - T_{MF}), \quad (5.33)$$

and $\zeta(x)$ is the Riemann ζ -function.

D. Microscopic calculation of the coefficients in the Free energy and effective action.

Using the symmetry arguments of Sec. III or by the explicit calculation, one finds that the solution of the form (5.25) is not unique, and, in fact any order parameter of the form

$$\hat{\Delta}(\vec{n}) = \hat{\sigma}_z^{AB} \otimes \hat{Q} \left\{ \Delta_0(T) \hat{\mathcal{P}}(\vec{n}) + \Delta_1(T) \left[\mathbb{1} - \hat{\mathcal{P}}(\vec{n}) \right] \right\} \quad (5.34)$$

solves Eq. (5.23), i.e. the fluctuation effects, studied in Sec. IV, are important. Here 4×4 matrix \hat{Q} is given by Eqs. (3.2).

The free energy and the effective action describes the contribution of configurations of the order parameter slowly varying in time and space. The time and space

gradient terms describes the cost of creating an inhomogeneous configuration, whereas the anisotropy leads the certain modes to become massive. To calculate the latter ones it is sufficient to consider the homogeneous and time independent configurations of the order parameter \hat{Q} , see Eqs. (3.2), whereas to find the former, one has to expand in small gradients of \hat{Q} .⁵

1. Stiffness.

To find the gradient terms we expand the order parameter as

$$\begin{aligned} Q(\mathbf{r}) &= \hat{Q} \left[1 - \frac{1}{2} \delta \hat{Q}^2(\mathbf{r}) \right] + \delta \hat{Q}(\mathbf{r}); \\ \delta \hat{Q}(\mathbf{r}) &= \int \frac{d^2 k}{(2\pi)^2} e^{i\vec{k}\vec{r}} \delta \hat{Q}_{\mathbf{k}}. \end{aligned} \quad (5.35)$$

In order to preserve the constraints (3.2b) up to the second order perturbation theory in $\delta \hat{Q}$ we require

$$\begin{aligned} \hat{Q} &= \hat{Q}^\dagger; \quad \hat{Q} \delta \hat{Q} + \delta \hat{Q} \hat{Q} = 0; \\ \left(\mathbb{1}^{KK'} \otimes \hat{\tau}_z^s \right) \delta \hat{Q} \left(\mathbb{1}^{KK'} \otimes \hat{\tau}_z^s \right) &= -\delta \hat{Q}. \end{aligned} \quad (5.36)$$

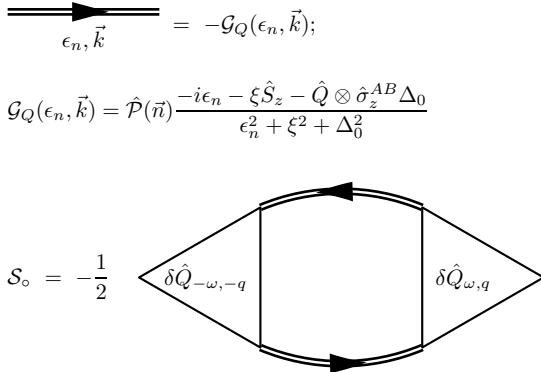


FIG. 16: Microscopic calculation of the stiffness and the collective modes velocity v_* in the effective action. Notation is defined in Eqs. (5.20) and (5.21).

Calculating the diagram on Fig. 16, we obtain for the

isotropic part of the Free energy

$$\begin{aligned} \mathbb{F}_o &= \frac{1}{2} \int \frac{d^2 q}{(2\pi)^2} T \sum_{\epsilon_m} \int \frac{d^2 k}{(2\pi)^2} \\ &\times \left[\text{Tr} \hat{G}_Q(\epsilon_m, \vec{k} + \vec{q}) \delta \hat{Q}_q \hat{G}_Q(\epsilon_m, \vec{k}) \delta \hat{Q}_{-q} \right. \\ &\quad \left. - \text{Tr} \hat{G}_Q(\epsilon_m, \vec{k}) \delta \hat{Q}_q \hat{G}_Q(\epsilon_m, \vec{k}) \delta \hat{Q}_{-q} \right], \end{aligned} \quad (5.37)$$

where ϵ_m are the fermionic Matsubara frequencies. The term in the last line is local and it comes from the interaction part of the Hamiltonian. Its explicit calculation is not necessary because $\delta Q_{\omega=0, k=0}$ corresponds to the motion along the degenerate manifold which can not produce any contribution to the Free energy – this requirement fixes the term unambiguously.

Expanding the Green functions in powers of small momentum q we find

$$\begin{aligned} \mathbb{F}_o &= -\frac{1}{4} \int \frac{d^2 q}{(2\pi)^2} T \sum_{\epsilon_m} \int \frac{d^2 k}{(2\pi)^2} \\ &\times \left[q^2 \sum_{\mu=x,y} \text{Tr} \partial_{k_\mu} \hat{G}_Q(\epsilon_m, \vec{k}) \delta \hat{Q}_q \partial_{k_\mu} \hat{G}_Q(\epsilon_m, \vec{k}) \delta \hat{Q}_{-q} \right], \end{aligned}$$

Then, the simple power counting shows that the integral is contributed by $\epsilon, vk \ll \mathcal{B}$ and therefore the integration rule (5.22) may be used. Finally, using the explicit expression for the Green function from Fig. 16 and Eq. (5.36), we obtain after simple algebra

$$\begin{aligned} \mathbb{F}_o &= \frac{\rho_K(T)}{8} \text{Tr} \int d^2 r (\nabla \hat{Q})^2; \\ \rho_K(T) &= \frac{\mathcal{B}}{4\pi} f_\rho \left(\frac{\Delta_0}{2\pi T} \right), \end{aligned} \quad (5.38)$$

where

$$\begin{aligned} f(x) &= \sum_{n=0}^{\infty} \frac{x^2}{((n+1/2)^2 + x^2)^{3/2}} \\ &\approx \begin{cases} 1 - \pi x e^{-2\pi x} + \mathcal{O}(e^{-4\pi x}), & x \gg 1 \\ 7\zeta(3)x^2 - \frac{93\zeta(5)}{2}x^4 + \mathcal{O}(x^6), & x \ll 1, \end{cases} \end{aligned} \quad (5.39)$$

and $\zeta(x)$ is the Riemann ζ -function.

As we have already explained, keeping the imaginary time derivative terms is valid only for $\Delta(T) \gg T$. At such low temperatures we find

$$\rho_K = \frac{\mathcal{B}}{4\pi} \quad (5.40)$$

independently of any logarithmic renormalization from higher energies.

In the opposite case, $\Delta(T) \ll T$ only constant in time fluctuations are important and we obtain $\mathcal{S}_o = \mathbb{F}_o/T$, where \mathbb{F}_o is given by Eq. (4.4a) and the stiffnesses on the mean-field correlation length, ξ_{MF} see Eq. (4.3), are given by

$$\rho_K(\xi_{MF}) = \rho_s(\xi_{MF}) = \frac{\mathcal{B}}{2\pi} \left(\frac{T_{MF} - T}{T_{MF}} \right). \quad (5.41)$$

where we used Eq. (5.33).

⁵ In principle one can perform the gauge transformation $\hat{Q} \rightarrow \hat{U} \hat{Q} \hat{U}^\dagger = \hat{S}_x$, and expand the fermionic determinant in terms of the non-abelian scalar, $\hat{U}^\dagger \partial_\tau \hat{U}$, and vector, $\hat{U}^\dagger \partial_\mu \hat{U}$, potentials. We have chosen not to do it here to avoid careful considerations of the terms arising from the non-gauge invariant integration cut-off in Eq. (5.22).

2. Leading anisotropies

The quadratic anisotropies (4.4b) arises both due to the warping of the single electron spectrum (2.13) and the short-range interactions (2.14). The diagrammatic calculation of these anisotropies is straightforward and it is shown on Fig. 17 a).

$$\text{Hexagon} = \frac{\lambda_w(R_B)\mathcal{B}}{2}\hat{\Lambda}_z [(n_x + in_y)^2 (\hat{\Sigma}_x + i\hat{\Sigma}_y) + h.c.];$$

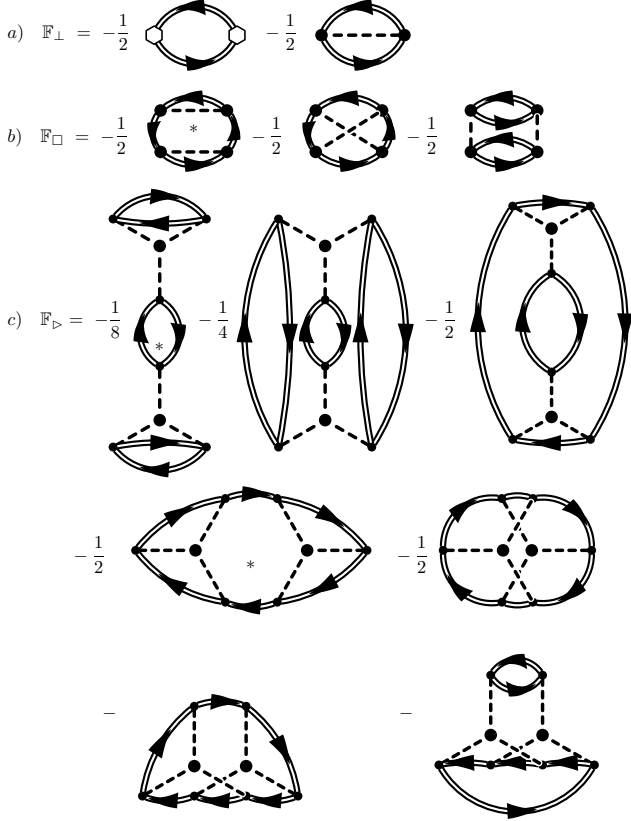


FIG. 17: Microscopic calculation of the anisotropic terms in the free energy. Diagrams containing largest power of $\ln(\mathcal{B}/\Delta_0)$ are marked by star.

We find $\mathbb{F}_\perp = \mathbb{F}_\perp^{(1)} + \mathbb{F}_\perp^{(2)}$ where the first contribution is due to the warping

$$\mathbb{F}_\perp^{(1)} = -\text{Tr} \hat{Q} \hat{\Lambda}_z \hat{Q} \hat{\Lambda}_z \frac{\lambda_w^2(R_B)\mathcal{B}^3}{16\pi v^2(R_B)} f_\rho \left(\frac{\Delta_0}{2\pi T} \right), \quad (5.42a)$$

where f_ρ is given by Eq. (5.39).

The second diagram of Fig. 17 b) describes the effect of the short range interaction (2.14). We take into account only the most relevant terms as specified in Eq. (5.12b). Term proportional to J_-^Σ do not contain the inter-valley Λ -matrices and, thus, do not cause the anisotropy. We

find

$$\mathbb{F}_\perp^{(2)} = - \left[F_-^z(R_B) \text{Tr} \left(\hat{Q} \hat{\Lambda}_z \right)^2 + F_-^\perp(R_B) \sum_{\mu=x,y} \text{Tr} \left(\hat{Q} \hat{\Lambda}_\mu \right)^2 \right] \times R_B v(R_B) \left[T \sum_n \int \frac{\mathcal{B} d\xi}{2\pi v^2(R_B)} \frac{\Delta_0(T)}{\epsilon_n^2 + \xi^2 + \Delta_0(T)^2} \right]^2. \quad (5.42b)$$

The logarithmic integral in Eq. (5.42b) is eliminated using Eq. (5.26), and we obtain Eq. (4.4b) at the scale $r_0 = \xi_{MF}$, see Eq. (4.3), with the couplings

$$\eta_z = -\mathcal{B} \left\{ \frac{\lambda_w^2(R_B)\mathcal{B}^2}{2\pi\Delta_0(0)^2} \left[\frac{\Delta_0^2(0)}{\Delta_0^2(T)} f_\rho \left(\frac{\Delta_0(T)}{2\pi T} \right) \right] + 2F_-^z(R_B) \left(\frac{2N}{\pi f_\Delta \left(\frac{\pi}{4g(R_B)} \right)} \right)^2 \right\}; \quad (5.43a)$$

$$\eta_\perp = -2\mathcal{B} F_-^\perp(R_B) \left(\frac{2N}{\pi f_\Delta \left(\frac{\pi}{4g(R_B)} \right)} \right)^2 \quad (5.43b)$$

where $f_\Delta(x)$ is defined in Eq. (5.28).

Equations (5.43) give complete expressions for the anisotropies in the free energy (4.4b) in terms of the microscopic coupling constants defined on the scale R_B . Equations (5.9), (5.12), (5.13), (5.4), (5.18), (5.19), (5.28), and (5.29) enable us to find the magnetic field dependence of the anisotropy constants. In the case of the strong magnetic field $\mathcal{B} \gtrsim \mathcal{B}_0$, see Eq. (5.17), it yields

$$\eta_z \approx -\mathcal{B} \left\{ \lambda_w^2(\mathcal{R}) \left(\frac{68\mathcal{B}}{\mathcal{B}_0} \right)^{3.9} \left[\frac{\Delta_0^2(0)}{\Delta_0^2(T)} f_\rho \left(\frac{\Delta_0(T)}{2\pi T} \right) \right] + 12.9 F_-^z(\mathcal{R}) \right\};$$

$$\eta_\perp \approx -12.9\mathcal{B} F_-^\perp(\mathcal{R}). \quad (5.44a)$$

For the weak magnetic field, $\mathcal{B} \lesssim \mathcal{B}_0$, we find

$$\eta_z \approx -\mathcal{B} \left\{ \lambda_w^2(\mathcal{R}) \left(\frac{\mathcal{B}}{5.1\mathcal{B}_0} \right)^2 \exp \left(\frac{\pi [\ln \frac{\mathcal{B}_0}{\mathcal{B}} + 6.28]}{2 \ln [\ln \frac{\mathcal{B}_0}{\mathcal{B}} + 6.28]} \right) \times \left[\frac{\Delta_0^2(0)}{\Delta_0^2(T)} f_\rho \left(\frac{\Delta_0(T)}{2\pi T} \right) \right] \left[0.15 \ln \left(\frac{\mathcal{B}_0}{\mathcal{B}} \right) + 1 \right]^{-13/4} + 12.9 F_-^z(\mathcal{R}) \left(\frac{\mathcal{B}}{\mathcal{B}_0} \right) \left[0.15 \ln \left(\frac{\mathcal{B}_0}{\mathcal{B}} \right) + 1 \right]^4 \right\};$$

$$\eta_\perp \approx -12.9\mathcal{B} F_-^\perp(\mathcal{R}) \left(\frac{\mathcal{B}}{\mathcal{B}_0} \right) \left[0.15 \ln \left(\frac{\mathcal{B}_0}{\mathcal{B}} \right) + 1 \right]^4. \quad (5.44b)$$

Comparison of the anisotropies from Eqs. (5.44) with the expressions for stiffness (5.41) together with the estimates $F_-^{z,\perp}(\mathcal{R}) \simeq 1$ indicates that the weak anisotropy

case is possible only for $\mathcal{B} \ll \mathcal{B}_0$ and at the strong magnetic field the anisotropy is dominating already at the mean-field correlation length, see Sec. IV C.

The very peculiar situation arises if $F_-^z(\mathcal{R}) < 0$, as we explained before, the value and the sign of this constant is determined by the details at the distances of the order of the lattice constant. In this case the exchange and the warping produce the contribution of the different sign and intersection of the Heisenberg line, $\eta_z > 0$, $|\eta_\perp| = |\eta_z|$, see Sec. (IV B 2) becomes possible. Using Eq. (5.44a), and estimates (5.10) and (5.13), we find the estimate for such field \mathcal{B}_H

$$\mathcal{B}_H \simeq 10^{-2} \mathcal{B}_0 \left(\frac{|F_-^z(\mathcal{R}) + |F_-^\perp(\mathcal{R})||}{\lambda_w^2(\mathcal{R})} \right)^{0.26} \approx 1 \div 10 \mathcal{B}_0 \gtrsim \mathcal{B}_0. \quad (5.45)$$

The manifestation of this line on the phase diagram will be considered in Sec. V E.

Calculation of the other anisotropies is self-explanatory from diagrams Fig. 17 b-c). Though, formally, they are of the same order in perturbation theory, they still can be classified in powers of $\ln(\mathcal{B}/\Delta) \ll 1$. Taking into account only the leading logarithmic contributions, and reexpressing the logarithmic expression using the mean-field equation (5.26), we find for anisotropy coefficients in Eqs. (4.4c) – (4.4d)

$$\kappa(\xi_{MF}) = \frac{\mathcal{B}}{2\pi} \left(\frac{N [F_-^\perp(\mathcal{R}) - 3J_\perp^\Lambda(\mathcal{R})]}{\pi f_\Delta \left(\frac{\pi}{4g(R_B)} \right)} \right)^2 f_\rho \left(\frac{\Delta_0(T)}{2\pi T} \right); \quad (5.46a)$$

$$\zeta(\xi_{MF}) = \frac{2\mathcal{B}}{\pi} [\mathcal{F}_-(\mathcal{R})]^2 D \left[\frac{N}{\pi f_\Delta \left(\frac{\pi}{4g(R_B)} \right)} \right] \times \left(\frac{\Delta_0(T)}{\Delta_0(0)} \right)^2 f_\rho \left(\frac{\Delta_0(T)}{2\pi T} \right), \quad (5.46b)$$

where $D(x) = xe^{-x}$, the functions $f_{\rho,\Delta}$ are defined in Eqs. (5.39) and (5.28). Deriving Eq. (5.46a), we took into account that κ is important only if $\eta_\perp \rightarrow 0$, see Sec. IV B 1. Thus, the irrelevant constants, see Eqs. (5.12a) had to be taken into account.

Expressions (5.46) together with Eqs. (5.12a) and (5.15) shows that those anisotropies are very small, so we will not analyse their asymptotics further.

E. Phase diagram in \mathcal{B} - T plane.

This subsection combines the symmetry analysis of Sec. IV with the microscopic calculation of the Free energy couplings in Sec. V D. As the result, we will construct the phase diagram in the plane determined by the Zeeman splitting \mathcal{B} and by the system temperature, T . As we have discussed in Sec. IV, the interesting phase transitions are determined by the thermal fluctuations

and it is convenient to introduce dimensionless Ginzburg-Levanyuk parameter

$$Gi \equiv \frac{4T_{MF}}{\mathcal{B}} \ll 1, \quad (5.47)$$

characterising strength of such fluctuations. Here the mean-field transition temperature is given by Eqs. (5.31) and (5.27) – (5.29).

Apparently, not all the regions of the phase diagram of Fig. 9 can be explored by varying \mathcal{B}, T and we will restrict ourselves with two most realistic, as we believe, cases. Namely, we assume that the absolute values of the interaction constants $|F_-^{z,\perp}(a)| \simeq 1$. For the sake of concreteness, we assume $F_-^\perp(a) > 0$. [Case of $F_-^\perp(a) < 0$ is obtained by the replacement $N_1 \leftrightarrow N_4$.]

Let us consider first the case of $F_-^z < 0$. Then, according to Eqs. (5.43), one finds $\eta_{z,\perp} < 0$. Mean-field diagram obtained from Fig. 4 is trivial and includes the continuous transition from the disordered normal state, to the spin-flux state, Fig. 3 (d), of the excitonic insulator, see Fig. 18.

The fine structure of the phase diagram, Fig. 18 (b), is obtained from the general Fig. 9, by using the microscopic expression for the Free energy couplings derived in Sec. V D. The topological structure of the phase diagram is most easily obtained by the mapping of the paths in \mathcal{B}, T plane to the path in (η_z, η_\perp) plane as shown in Fig. 18 (c).

The positions of the transitions lines on the phase diagrams are obtained by combining the phenomenological results of Sec. IV and the microscopic analysis of Sec. V D.

For instance, using Eqs. (4.15) and (5.41), we obtain in the limit of the small vortex fugacity

$$\frac{T_{MF} - T}{T_{MF} Gi} \approx \begin{cases} 4; & \text{line (i);} \\ 1; & \text{line (ii).} \end{cases} \quad (5.48a)$$

Analogously, using Eqs. (4.20), (4.14) and (5.44b) we obtain a position of the Ising line. With the logarithmic accuracy, we find for line (iii) of Fig. 18 (b):

$$\frac{T_{MF} - T}{T_{MF} Gi} \approx \begin{cases} \frac{1}{4} \ln \frac{\mathcal{B}_0 Gi}{\mathcal{B}}; & \mathcal{B}_0 \exp(-1/Gi) \lesssim \mathcal{B} \ll \mathcal{B}_0 Gi \\ \rightarrow 0; & \mathcal{B} \gtrsim \mathcal{B}_0 Gi. \end{cases} \quad (5.48b)$$

Case of $F_-^z < 0$ is more sophisticated. As we noticed in Sec. V D, coefficient η_z changes its sign as the function of the magnetic field and at some point crosses the Heisenberg line at field \mathcal{B}_H . At the mean-field level, it corresponds to the continuous transition between two-kinds of excitonic insulator: spin flux state, see Fig. 3 (d), and the link centered spin density wave, see Fig. 3 (b,c).

Similarly to the previous case, the fine structure of the phase diagram, Fig. 19 (b), is obtained from the general Fig. 9, by the mapping of the paths in \mathcal{B}, T plane to the path in (η_z, η_\perp) plane as shown in Fig. 19 (c).

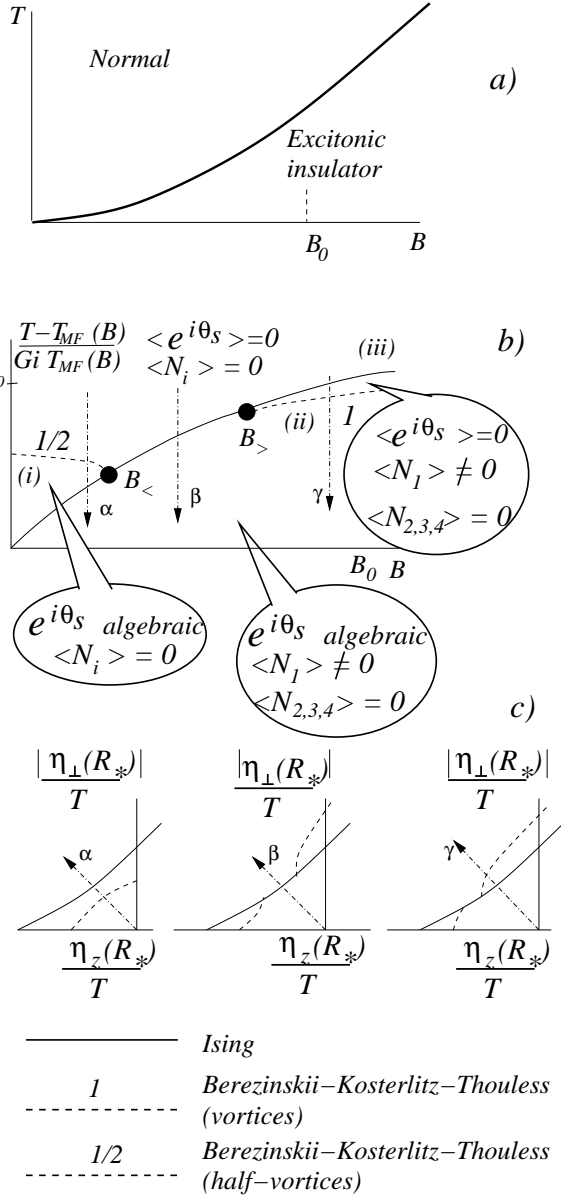


FIG. 18: Phase diagram of the graphene in the parallel magnetic field for the short range interaction constant $F^z > 0$. a) Mean field structure of the phase diagram; b) The “fine” structure of the phase diagram in the close vicinity of the mean-field transition temperature, $T_{MF}(\mathcal{B})$; c) Relation of the phase diagram (b) to the more general phenomenological phase diagram of Fig. 9.

The Berezinskii-Kosterlitz-Thouless transition lines (i), (ii) on Fig. 19 (b) are still determined by the expressions (5.48a). Ising line (iv) Berezinskii-Kosterlitz-Thouless line and the are found from Eqs. (4.40) and (5.41). Expanding

$$\Delta\eta \approx \left(\frac{B - B_H}{B_H} \right) \eta_{\perp}$$

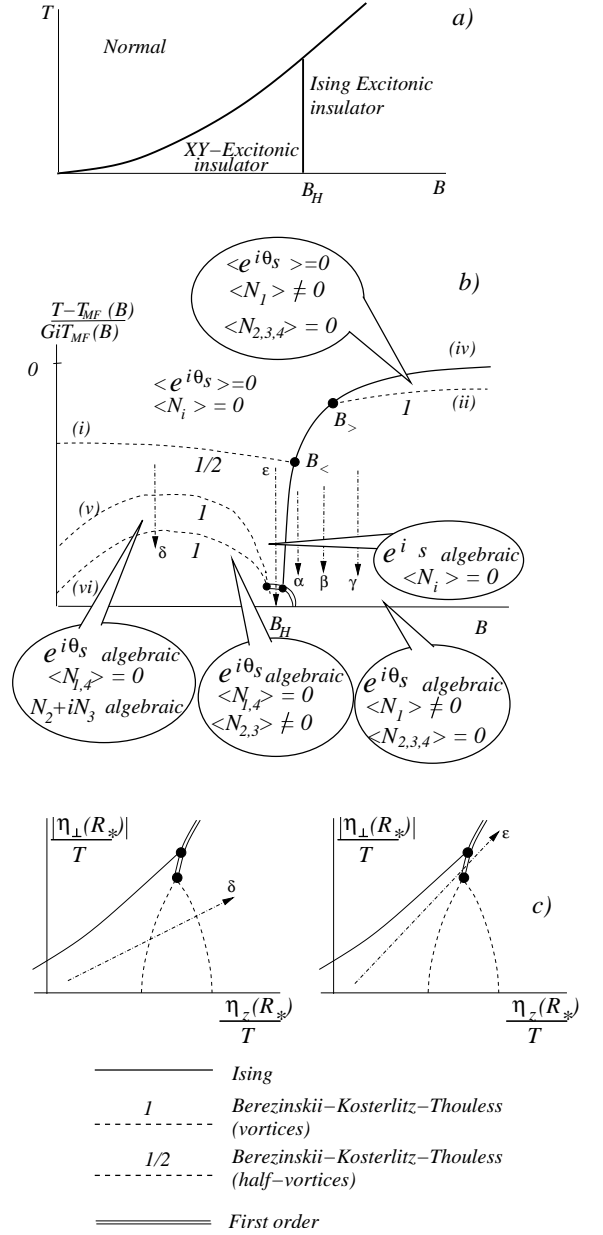


FIG. 19: Phase diagram of the graphene in the parallel magnetic field for the short range interaction constant $F^z < 0$. a) Mean field structure of the phase diagram; b) The “fine” structure of the phase diagram in the close vicinity of the mean-field transition temperature, $T_{MF}(\mathcal{B})$; c) Relation of the phase diagram (b) to the more general phenomenological phase diagram of Fig. 9. Cross-section denoted by α, β, γ are shown on Fig. 18 c).

we obtain with the logarithmic accuracy for $\mathcal{B}_H \exp(-Gi) \ll |\mathcal{B} - \mathcal{B}_H| \ll \mathcal{B}_H$:

$$\frac{T_{MF} - T}{T_{MF} Gi} \approx \begin{cases} \frac{1}{8} \ln \frac{\mathcal{B}_H}{\mathcal{B} - \mathcal{B}_H}; & \text{line (iv);} \\ \frac{1}{8} \ln \frac{\mathcal{B}_H}{\mathcal{B}_H - \mathcal{B}}; & \text{line (v).} \end{cases} \quad (5.49a)$$

For larger \mathcal{B} the Ising line (iv) approaches the mean-field temperature. The Berezinskii-Kosterlitz-Thouless transitions lines (v), for $\mathcal{B} \ll \mathcal{B}_H$ can be found using Eqs. (4.20), (4.14), and (5.44b). For the fields $\mathcal{B}_0 \exp(-1/Gi) \lesssim \mathcal{B} \ll \mathcal{B}_0 Gi$ this yields

$$\frac{T_{MF} - T}{T_{MF} Gi} \approx \frac{1}{4} \ln \frac{\mathcal{B}_0 Gi}{\mathcal{B}}; \quad \text{line(v)}; \quad (5.49b)$$

The Berezinskii-Kosterlitz-Thouless line (vi) turns out to lie outside the fluctuation region due to the large numerical factor in Eq. (4.44) and smallness of ζ in Eq. (5.46b). We will not write-down its asymptotic behaviour.

This completes our analysis of the structure of the phase diagram of graphene in the parallel magnetic field, characterised by the Zeeman splitting \mathcal{B} .

VI. SUMMARY AND CONCLUSIONS

In this paper we have discussed two problems concerning clean graphene: (i) possible effects of in-plane magnetic field in facilitating a formation of excitonic condensate and (ii) a role of the long range Coulomb interaction and its influence on other interactions in the system. The second topic is more general than the first and has a broader significance, though, as far the paper goes, it was discussed in the second part.

In zero magnetic field graphene is a gapless semiconductor with two Fermi points in the Brillouin zone (valleys). In-plane magnetic field pushes up- and down-spin bands in opposite directions transforming the system into a metal with extended Fermi surfaces for electrons and holes of opposite spin. There are two such Fermi surfaces corresponding to two possible valley indices. Electrons and holes attract through the Coulomb interaction which creates a possibility of exciton condensation along the lines first described by Keldysh and Kopaev¹¹. The maximal possible symmetry of the order parameter is U(2), lattice effects bring it down to U(1). The system in its low temperature phase is an insulator with a gapless collective mode corresponding to fluctuations of spin density in the directions transverse to the applied magnetic field. The above is a brief summary of the discussion of Sections II-IV. Section IV also contains a detailed phase diagram. The discussion in these sections dealt with the Landau-Ginzburg free energy functional written purely on symmetry grounds where various energy scales of the system enter as parameters.

Section V contains a microscopic analysis tailored especially for graphene. The ultimate goal was to obtain estimates for the critical temperature and various parameters of the phase diagram, but a byproduct of the analysis is a study of how the strongest interaction in graphene - the Coulomb interaction affects the spectrum and renormalizes other interactions (such as the short range exchange). As is well known, the Coulomb interaction in graphene, measured by its dimensionless value $g = \pi e^2/2v$ is quite strong at energies of the order of

the bandwidth. We have found, however, that the effective coupling steadily diminishes at low energies and asymptotically vanishes at $E = 0$. The scale dependence of g is rather slow and is given by Eq.(5.4). This formula includes an important scale \mathcal{R} , which we estimate for graphene as being of order of $10^2 - 10^3$ lattice constants. This scale separates the region of relatively strong interaction where $g(r)$ decreases as a power law, from the region of weak coupling where $g(r) \sim [\ln r]^{-1}$. It also sets the scale \mathcal{B}_0 for the magnetic field (5.17)[our estimate is $\mathcal{B}_0 \approx 10 - 100\text{K}$].

The renormalization process is drastically altered at energies of order of the applied magnetic field \mathcal{B} . The field sets the ultraviolet cut-off for the physics of excitonic insulator. However, the upper cut-off for its collective excitations is much lower and is set by the value of the mean field gap Δ_0 . One may anticipate that the latter energy scale is exponentially small in comparison with the cut-off \mathcal{B} . This is indeed the case, but fortunately the inverse coupling constant $1/g(r \sim \mathcal{B}^{-1})$, which stays in the exponent, depends rather weakly on the magnetic field [see (5.29a,5.29b)] so that the magnitude of Δ_0 is not that small. Our estimate is that in fields of the order of or stronger than 10T the mean field temperature is $T_{MF} \leq 10^{-3}\mathcal{B}$. This makes it possible to observe the excitonic effects described in this paper in the temperature range of tens of mK (see more discussion in Section V C).

Though the long range Coulomb interaction is certainly the main player, its renormalization drags with itself weaker interactions, such as the short range exchange, strengthening them at low energies. Such interactions break the U(2) symmetry present at low energies when only the long range Coulomb interaction is taken into account. The analysis of Section V C.2 demonstrates that the U(2) symmetry survives in the excitonic insulator only at $\mathcal{B} \ll \mathcal{B}_0$ when the estimated transition temperatures are probably too low for the effect to be observed. In the realistic region $\mathcal{B} \geq \mathcal{B}_0$ the anisotropy is strong. The expected phase diagrams in $\mathcal{B} - T$ plane are given on Figs. 18,19 [they differ by a sign of a certain interaction parameter which on the current stage remains unknown]. Strong fields of order of 10T or more, which are required to make the excitonic insulator observable at temperatures above tens of mK, will probably put one in the regime marked by β or γ on the phase diagram Figs. 18, 19. The spin configuration corresponding to this regime is depicted on Fig. 3 d) and corresponds to the spin-flux phase.

Acknowledgments

AMT was supported by the DOE under contract number DE-AC02 -98 CH 10886. We acknowledge inspirational conversations with I. Zaliznyak, and interesting discussions with L. Levitov, D. Khveshchenko, and M. Foster.

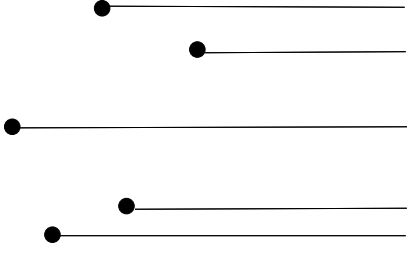


FIG. 20: Cuts on the $x-y$ plane attached to each topological defect in the five-vortex configuration.

APPENDIX A: DERIVATION OF EQ. (4.11).

Let us re-write Eq. (4.4a') in a form

$$\mathbb{F}_\circ = \frac{\rho_K}{4} \text{Tr} \hat{j}_\mu^2 + \frac{\rho_s - \rho_K}{8} \left[\text{Tr} \hat{j}_\mu \right]^2, \quad (\text{A1})$$

where

$$\hat{j}_\mu \equiv -i \hat{V}^\dagger \partial_\mu \hat{V}. \quad (\text{A2})$$

The topological defects (4.7) and (4.9) are determined by the condition

$$\frac{1}{2\pi} \oint dx_\mu \text{Tr} \hat{j}_\mu = \pm 1; \pm \frac{1}{2}, \quad (\text{A3})$$

i.e.

$$\theta = \frac{-i}{2} \text{Tr} \ln \hat{V} \quad (\text{A4})$$

must be multi-valued function of the coordinate.

In order to avoid the consideration of the multi-valued field we introduce cuts parallel to, say, x axis connecting each vortex or half-vortex with the boundary of the system [any physical quantity, obviously, does not depend on the choice of the cut], see Fig. 20, and consider all the matrices to be single valued function but the phases experiencing the discontinuity on the cuts.

The current (A2) should be continuous thus we modify the definition as

$$\begin{aligned} \hat{j}_x &= -i \hat{V}^\dagger \partial_x \hat{V}; \\ \hat{j}_y &= -i \hat{V}^\dagger \partial_y \hat{V} + \pi \sum_{j=1}^{\mathcal{N}^{(1)}} l_j^{(1)} \delta(y - y_j^{(1)}) \text{sgn}(x - x_j^{(1)}) \\ &\quad + \pi \sum_{j=1}^{\mathcal{N}^{(1/2)}} l_j^{(1/2)} \frac{1 + \mathbf{m}_j \cdot \boldsymbol{\sigma}}{2} \delta(y - y_j^{(1/2)}) \text{sgn}(x - x_j^{(1/2)}); \end{aligned} \quad (\text{A5})$$

where $\mathcal{N}^{(1)}$ and $\mathcal{N}^{(1/2)}$ are the number of the vortices and the vertices respectively, x_j, y_j are their coordinates, $l_j = \pm 1$ is the corresponding vorticity and \mathbf{m}_j is the unit vector characterising the spin of the j th half-vortex.

Writing the summation over the vortex and half-vortex coordinates explicitly, we obtain

$$\begin{aligned} \mathcal{Z} &\propto \sum_{\mathcal{N}^{(1)}=0}^{\infty} \frac{\mu_1^{\mathcal{N}^{(1)}}}{\mathcal{N}^{(1)}!} \prod_{j=1}^{\mathcal{N}^{(1)}} \sum_{l_j^{(1)}=\pm 1} \int \frac{dx_j^{(1)} dy_j^{(1)}}{r_0^2} \sum_{\mathcal{N}^{(1/2)}=0}^{\infty} \frac{\mu_{1/2}^{\mathcal{N}^{(1/2)}}}{\mathcal{N}^{(1/2)}!} \prod_{j=1}^{\mathcal{N}^{(1/2)}} \sum_{l_j^{(1/2)}=\pm 1} \int \frac{dx_j^{(1/2)} dy_j^{(1/2)} d\mathbf{m}_j}{4\pi r_0^2} \int \mathcal{D}\hat{V} \\ &\quad \times \exp \left\{ - \int dx dy \left[\frac{\rho_K}{4T} \text{Tr} \hat{j}_\mu^2 + \frac{\rho_s - \rho_K}{8T} \left(\text{Tr} \hat{j}_\mu \right)^2 \right] \right\}, \end{aligned} \quad (\text{A6})$$

where the matrix current \hat{j}_μ is given by Eq. (A5).

After introducing the dual 2×2 matrix field $\hat{h} = \hat{h}^\dagger$, Eq. (A6) acquires the form

$$\begin{aligned} \mathcal{Z} &\propto \sum_{\mathcal{N}^{(1)}=0}^{\infty} \frac{\mu_1^{\mathcal{N}^{(1)}}}{\mathcal{N}^{(1)}!} \prod_{j=1}^{\mathcal{N}^{(1)}} \sum_{l_j^{(1)}=\pm 1} \int \frac{dx_j^{(1)} dy_j^{(1)}}{r_0^2} \sum_{\mathcal{N}^{(1/2)}=0}^{\infty} \frac{\mu_{1/2}^{\mathcal{N}^{(1/2)}}}{\mathcal{N}^{(1/2)}!} \prod_{j=1}^{\mathcal{N}^{(1/2)}} \sum_{l_j^{(1/2)}=\pm 1} \int \frac{dx_j^{(1/2)} dy_j^{(1/2)} d\mathbf{m}_j}{4\pi r_0^2} \int \mathcal{D}\hat{V} \mathcal{D}\hat{h} \\ &\quad \times \exp \left\{ - \int dx dy \left[\frac{\rho_K}{4T} \text{Tr} \hat{j}_x^2 + \frac{T}{4\rho_K} \text{Tr} \left(\partial_x \hat{h} \right)^2 + \frac{\rho_s - \rho_K}{8T} \left(\text{Tr} \hat{j}_x \right)^2 + \left(\frac{T}{8\rho_s} - \frac{T}{8\rho_K} \right) \left(\text{Tr} \partial_x \hat{h} \right)^2 + i \text{Tr} \hat{j}_y \partial_x \hat{h} \right] \right\}, \end{aligned} \quad (\text{A7})$$

Substituting Eq. (A5) into Eq. (A7), integrating the terms with δ functions by parts and summing over l_j , we find

$$\begin{aligned} \mathcal{Z} \propto & \int \mathcal{D}\hat{V}\mathcal{D}\hat{h} \sum_{\mathcal{N}^{(1)}=0}^{\infty} \frac{\mu_1^{\mathcal{N}^{(1)}}}{\mathcal{N}^{(1)}!} \prod_{j=1}^{\mathcal{N}^{(1)}} \int \frac{dx_j^{(1)} dy_j^{(1)}}{r_0^2} 2 \cos \pi \text{Tr} \hat{h}(r_j^{(1)}) \\ & \times \sum_{\mathcal{N}^{(1/2)}=0}^{\infty} \frac{\mu_{1/2}^{\mathcal{N}^{(1/2)}}}{\mathcal{N}^{(1/2)}!} \prod_{j=1}^{\mathcal{N}^{(1/2)}} \int \frac{dx_j^{(1/2)} dy_j^{(1/2)} d\mathbf{m}_j}{4\pi r_0^2} 2 \cos \pi \left[\text{Tr} \hat{h}(r_j^{(1/2)}) \frac{1 + \mathbf{m}_j \cdot \vec{\sigma}}{2} \right] \\ & \times \exp \left\{ - \int dx dy \left[\frac{\rho_K}{4T} \text{Tr} \partial_x \hat{V}^\dagger \partial_x \hat{V} + \frac{T}{4\rho_K} \text{Tr} \left(\partial_x \hat{h} \right)^2 + \frac{\rho_s - \rho_K}{8T} \left(-i \text{Tr} \hat{V}^\dagger \partial_x \hat{V} \right)^2 \right. \right. \\ & \left. \left. + \left(\frac{T}{8\rho_s} - \frac{T}{8\rho_K} \right) \left(\text{Tr} \partial_x \hat{h} \right)^2 + \text{Tr} \hat{V}^\dagger \partial_y \hat{V} \partial_x \hat{h} \right] \right\}. \end{aligned} \quad (\text{A8})$$

After the summation over $\mathcal{N}^{(1/2)}$, $\mathcal{N}^{(1)}$, and integration over \mathbf{m}_j , we obtain Eq. (4.11).

APPENDIX B: ANALYSIS OF THE ISING PHASE TRANSITION.

In the vicinity of $T = \pi\rho_K$, where the mutually dual cosines have the same scaling dimension 1, partition (4.25) can be mapped to the quantum many-body problem at zero temperature and then refermionized. The reader can consult Ref. 23 where the necessary information about 2D Ising model is provided. Choosing y coordinate for imaginary time, we re-write the classical Eq. (4.25)

$$\begin{aligned} \mathcal{Z} \propto & \text{Tr} \exp \left(-L_y \int dx \hat{\mathcal{H}} \right) \\ \hat{\mathcal{H}} = & \frac{\rho_K}{2T} \left(\partial_x \hat{\phi} \right)^2 + \frac{T}{2\rho_K} \left(\partial_x \hat{\theta} \right)^2 \\ & + \frac{\eta_\perp}{R_*^2 T} \cos 2\hat{\phi} + \frac{\mu_{14}}{R_*^2} \cos \left(2\pi\hat{\theta} \right), \\ \left[\partial_x \hat{\phi}(x); \hat{\theta}(x') \right] = & i\delta(x - x') \end{aligned} \quad (\text{B1})$$

Then using the fermionization rules

$$\begin{aligned} \hat{R}(x) \propto & \exp \left[i\hat{\phi}(x) + i\pi\hat{\theta} \right]; \\ \hat{L}(x) \propto & \exp \left[-i\hat{\phi}(x) + i\pi\hat{\theta} \right]; \end{aligned} \quad (\text{B2})$$

we write down the corresponding 1D quantum fermionic Hamiltonian density as

$$\begin{aligned} \hat{\mathcal{H}} = & i(L^+ \partial_x L - R^+ \partial_x R) + (\pi T/\rho_K - 1)R^+ R L^+ L \\ & + \eta_\perp (R^+ L + L^+ R) + \mu_{34}(R^+ L^+ + L R) \end{aligned} \quad (\text{B3})$$

It is convenient to decompose the Dirac spinor into the real (Majorana) components:

$$R = r_1 + ir_2, \quad L = l_1 + il_2 \quad (\text{B4})$$

where the corresponding operators are real ($r_a = r_a^+$, $l_a = l_a^+$) and satisfy the following commutation relations:

$$\begin{aligned} \{r_a(x_1), r_b(x_2)\} &= \delta_{ab} \delta(x_{12}), \\ \{l_a(x_1), l_b(x_2)\} &= \delta_{ab} \delta(x_{12}), \{r_a(x_1), l_b(x_2)\} = 0 \end{aligned} \quad (\text{B5})$$

Then Eq. (B3) becomes

$$\begin{aligned} \mathcal{H} = & \frac{i}{2} (l_a \partial_x l_a - r_a \partial_x r_a) + \tau (l_1 r_1) (l_2 r_2) \\ & i(\eta_\perp/T + \mu_{34}) r_1 l_1 + i(\eta_\perp/T - \mu_{34}) r_2 l_2 \end{aligned} \quad (\text{B6})$$

where $\tau = [T/(\pi\rho_K) - 1]$. Hamiltonian (B6) describes two quantum Ising models coupled by the energy density operators. The original order parameter operator can be expressed in terms of order and disorder parameters of the Ising models σ and μ , see Ref. 23 for the corresponding definitions:

$$e^{i\phi} = \sigma_1 \sigma_2 + i\mu_1 \mu_2 \quad (\text{B7})$$

The sign of Majorana mass in the Ising model plays an important role determining what operator (σ or μ) acquires a vacuum expectation value. Then from (B7) it is clear that this operator acquires a finite expectation value when the masses of the two species of Majorana fermions have the same sign so that either σ_a or μ_a fields condense simultaneously. The high temperature phase is characterised by masses of different sign.

At small $|\tau| \ll 1$ we can use perturbation theory to write the equations for the masses (let us choose $\eta_\perp > 0$):

$$\begin{aligned} m_1 &= (\eta_\perp/T + \mu_{34}) > 0; \\ m_2 &= (\eta_\perp/T - \mu_{34}) + \frac{\tau}{2\pi} m_1 \ln(1/R^* |m_1|); \end{aligned} \quad (\text{B8})$$

It follows that m_2 changes sign at

$$T_c/\pi\rho_K - 1 = \frac{\eta_\perp/T - \mu_{34}}{\eta_\perp/T + \mu_{34}} \ln \left(\frac{1}{R^*(\eta_\perp + \mu_{34})} \right) \quad (\text{B9})$$

where the second order phase transition from disordered (high temperature) to the ordered (low temperature) state takes place. Equation (B9) agrees with Eq. (4.29).

-
- ¹ K.S. Novoselov, A.K. Geim, S.V. Morozov, D. Jiang, Y. Zhang, S.V. Dubonos, I.V. Grigorieva, and A.A. Firsov, *Science* **306**, 666 (2004).
- ² For a recent progress review, see A.K. Geim and K.S. Novoselov, *Nature Materials* **6**, 183 (2007).
- ³ K.S. Novoselov, A.K. Geim, S.V. Morozov, D. Jiang, M.I. Katsnelson, I.V. Grigorieva, S.V. Dubonos, and A.A. Firsov, *Nature* **438**, 197 (2005).
- ⁴ Y. Zhang, Y.W. Tan, H.L. Stormer, and P. Kim, *Nature* **438**, 201 (2005).
- ⁵ D.V. Khveshchenko, *Phys. Rev. Lett.* **87**, 246802 (2001); D.V. Khveshchenko and H. Leal, *Nucl. Phys.* **B687**, 323 (2004); D.V. Khveshchenko and W.F. Shively, *Phys. Rev.* **B73**, 115104 (2006).
- ⁶ A.A. Abrikosov and S.D. Beneslavskii, *Sov. Phys. JETP* **32** 699 (1971).
- ⁷ J. Gonzalez, F. Guinea and M. A. H. Vozmediano, *Phys. Rev.* **B59**, R2474 (1999).
- ⁸ D. T. Son, *Phys. Rev. B* **75**, 235423 (2007).
- ⁹ For a general construction of the terms compatible with the lattice symmetries, see G.L. Bir and G.E. Pikus, *Symmetry and strain-induced effects in semiconductors*, New York, Wiley (1974).
- ¹⁰ We use parametrization as in I.L. Aleiner and K.B. Efetov, *Phys. Rev. Lett.* **97**, 236801 (2006).
- ¹¹ L.V. Keldysh and Y.V. KopaeV, *Sov. Phys. Solid State*, **6**, 2219 (1965).
- ¹² V.L. Berezinskii, *Sov. Phys. JETP*, **32**, 493 (1971).
- ¹³ J.M. Kosterlitz and D.J. Thouless, *J. Phys. C*, **5**, L124 (1972); *ibid.*, **6**, 1181 (1973).
- ¹⁴ A.A. Abrikosov, L.P. Gorkov, and I.E. Dzyaloshinskii, *Methods of Quantum Field Theory in Statistical Physics*, Prentice Hall, New York (1963).
- ¹⁵ Formula (5.9) for $r_c \gg \mathcal{R}$ was first obtained by I.L. Aleiner and V.I. Fal'ko (unpublished).
- ¹⁶ Detailed calculation of the polarization operator at finite doping can be found in B. Wunsch, T. Stauber, F. Sols, and F. Guinea, *New J. Phys.* **8**, **318** (2006). For our purposes it is important only that $\Pi(0, q)$ does not depend on the wavevector at all for $q < 2k_F$.
- ¹⁷ See *e.g.* Z. Jiang, E.A. Henriksen, L.C. Tung, Y.-J. Wang, M.E. Schwartz, M.Y. Han, P. Kim, and H.L. Stormer, *Phys. Rev. Lett.* **98**, 197403 (2007); R.S. Deacon, K.-C. Chuang, R.J. Nicholas, K.S. Novoselov, A.K. Geim, arXiv:0704.0410.
- ¹⁸ D.A. Abanin, P.A. Lee, and L.S. Levitov, *Phys. Rev. Lett.* **98**, 156801 (2007).
- ¹⁹ I.F. Herbut, *Phys. Rev. B*, **75** 165411 (2007).
- ²⁰ E. McCann, K. Kechedzhi, V.I. Fal'ko, H. Suzuura, T. Ando, and B.L. Altshuler, *Phys. Rev. Lett.* **97**, 146805 (2006).
- ²¹ This idea belongs to I. Zaliznyak (private communication).
- ²² In the mean-field picture, the existence of such lines and the points where three continuous phase transitions intersect are not possible [See §150 of L.D. Landau and E.M. Lifshits, *Statistical Physics*, Oxford, New York, Pergamon Press, (1986)] and the critical line $B_1 - B'_1$, see Fig. 5 a), becomes either the first order phase transition line or split into two second order phase transition line. The existence of this line is a consequence of the fluctuations making the vortex operator $\cos 2\pi h_s$ to vanish.
- ²³ A. M. Tsel'ik, "*Quantum Field Theory in Condensed Matter Physics*", Cambridge University Press, 2nd edition, 2003.